




## Particle-hole asymmetric lifetimes promoted by nonlocal spin and orbital fluctuations in SrVO<sub>3</sub> monolayers

Matthias Pickem <sup>\*</sup>, Jan M. Tomczak , and Karsten Held   
*Institute for Solid State Physics, TU Wien, Vienna 1040, Austria*

 (Received 19 January 2022; accepted 6 September 2022; published 30 September 2022)

The two-dimensional nature of engineered transition-metal ultrathin oxide films offers a large playground of yet to be fully understood physics. Here, we study pristine SrVO<sub>3</sub> monolayers that have recently been predicted to display a variety of magnetic and orbital orders. We find that nonlocal magnetic (orbital) fluctuations lead to a strong (weak to moderate) momentum differentiation in the self-energy, particularly in the scattering rate. In the one-band 2D Hubbard model, momentum selectivity on the Fermi surface (“ $k = k_F$ ”) is known to lead to pseudogap physics. Here instead, in the multiorbital case, we evidence a differentiation between momenta on the occupied (“ $k < k_F$ ”) and the unoccupied side (“ $k > k_F$ ”) of the Fermi surface. Based on the dynamical vertex approximation, and introducing a “binaural fluctuation diagnostics” tool, we advance the understanding of spectral signatures of nonlocal fluctuations. Our work calls to (re)examine ultrathin oxide films and interfaces with methods beyond dynamical mean-field theory and may point to correlation-enhanced thermoelectric effects.

DOI: [10.1103/PhysRevResearch.4.033253](https://doi.org/10.1103/PhysRevResearch.4.033253)

### I. INTRODUCTION

In the vicinity of phase transitions and in low-dimensional systems, nonlocal long-range fluctuations are known to proliferate. These are not only crucial for the critical behavior but may also lead to a strong enhancement of the scattering rate, i.e., a dampening of the quasiparticle lifetime. In three dimensions, it is still debated [1–3] whether this scattering rate is actually diverging at a phase transition or approaches a large but finite value. Even more peculiar is the situation in two dimensions. There, an actual phase transition—associated with the breaking of continuous symmetries—is prohibited. Nonetheless nonlocal long-range fluctuation may still become huge and can result in the famous pseudogap that has been experimentally observed in cuprate superconductors [4–7]. The pseudogap arises from a pronounced momentum differentiation of the scattering rate at low energy. It is largest in the antinodal direction where eventually a gap opens at low enough temperatures. One possible explanation are long-range *antiferromagnetic* spin fluctuations [8–13], with the momentum differentiation originating from the perfect antiferromagnetic nesting at the hot spots [1,14–18], from the vicinity to a van Hove singularity in the antinodal direction [18–21], or from the spin-fermion vertex turning complex at strong coupling [22]. It has also been suggested, on the basis of model studies, that a pseudogap phase can be driven by *ferromagnetic* fluctuations [23–27]. While pseudogap physics is mostly associated with cuprates, it has also been evidenced

in other layered materials [29]: iron pnictides [30–33] and chalcogenides [34], (layered) nickelates [35], and iridates [36]. However, the origin of momentum-differentiated scattering rates is far from understood.

Here, we study a material that is quasi-two-dimensional by engineering: a monolayer of SrVO<sub>3</sub>. In the bulk, SrVO<sub>3</sub> is a correlated paramagnetic metal [37,38] with a correlation-induced kink [39,40] linked to the effective Kondo temperature [41]. Grown as a film, it is known to undergo a metal-insulator transition below a critical thickness when deposited on an SrTiO<sub>3</sub> [42–44] or LSAT [45] substrate. We focus on a monolayer of SrVO<sub>3</sub> grown on the common SrTiO<sub>3</sub> substrate and consider two different terminations of the film to the vacuum: VO<sub>2</sub> and SrO, see insets of Fig. 1. Only the former has been evidenced experimentally [46], but it could be preferable to cover the films with a SrTiO<sub>3</sub> capping layer which leads to a structure more akin to the SrO termination. Such a capping layer also prevents a surface reconstruction with oxygen adatoms, which result in a dead surface layer [47], at least for slightly thicker films. A preceding study [28], based on dynamical mean-field theory (DMFT) [48–50], revealed a rich variety of orbital ordered and magnetic phases as a function of doping, see Fig. 1. Experimentally, the phase diagrams could be perused by applying a gate voltage.

In the present paper, we go beyond DMFT and study the effect of nonlocal fluctuations on spectral properties using the dynamical vertex approximation (DΓA) [51–54]. As for cuprates, we find that strong long-range fluctuations lead to a substantial momentum-dependence in the self-energy. In stark contrast to the cuprates, however, in ultrathin films of SrVO<sub>3</sub> the momentum differentiation does not distinguish momenta *on* the Fermi surface but those *perpendicular* to it. For example, for the SrO-termination and antiferromagnetic spin fluctuations [above the red dome in Fig. 1(a)], occupied states with momenta below the Fermi surface have a long, Fermi liquidlike lifetime. Instead, unoccupied states above the

<sup>\*</sup>matthias.pickem@gmail.com

Published by the American Physical Society under the terms of the [Creative Commons Attribution 4.0 International](https://creativecommons.org/licenses/by/4.0/) license. Further distribution of this work must maintain attribution to the author(s) and the published article’s title, journal citation, and DOI.

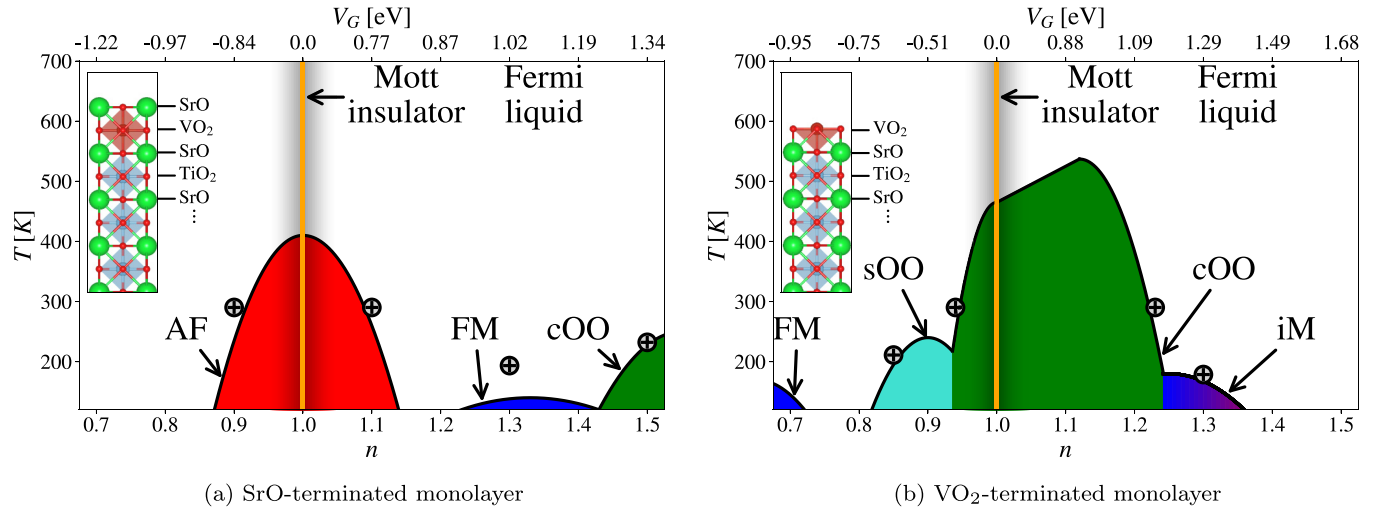


FIG. 1. Phase diagrams. (a) SrO- and (b) VO<sub>2</sub>-terminated SrVO<sub>3</sub> monolayer on top of a SrTiO<sub>3</sub> substrate (see insets for crystal structures) exhibit numerous phases as a function of electrons per site ( $n$ ; lower  $x$  axis) in the low-energy vanadium  $t_{2g}$  orbitals or gate voltage ( $V_G$ ; upper  $x$  axis): antiferromagnetism (AF: red), ferromagnetism (FM: blue), incommensurate magnetism (iM: blueish), checkerboard orbital order (cOO: green), and stripe orbital order (sOO: turquoise). The colored domes mark the occurrence of a long-range order within dynamical mean-field theory (DMFT); adapted from Ref. [28]. The “+”-marks indicate points for which we present D $\Gamma$ A (and DMFT) data in the present paper.

Fermi surface have short lifetimes and even kinks (downturns) in the self-energy, signaling a depletion of states. For orbital ordering and ferromagnetic fluctuations (above green and blue regions) it is vice versa. The same is true for the VO<sub>2</sub> termination and the most relevant  $xz/yz$  orbitals in the regime of orbital and incommensurate magnetic fluctuations above half-filling [ $n > 1$  in Fig. 1(b), above the green and blue regions]. Below half-filling, instead, nonlocal correlations only have a minor impact on the self-energy of this termination.

A pronounced asymmetry with respect to the Fermi surface in the *real part* of the self-energy is a common phenomenon, mostly owing to nonlocal exchange. For example, in *GW* calculations [55–57], it leads to larger semiconductor band gaps than in density functional theory. For the *imaginary part* of the self-energy (the scattering rate), however, such an asymmetry has, to the best of our knowledge, not been reported so far. The particle-hole asymmetric lifetimes arising here from a momentum-selectivity of renormalizations can complement more ubiquitous orbital-selective asymmetries and could drive large thermoelectric effects.

The outline of the paper is as follows. Section II provides information on the employed electronic structure methods. Section III presents the DMFT Fermi surfaces and spectral functions and the trends upon doping the SrVO<sub>3</sub> monolayer. Nonlocal fluctuations in ABINITIOD $\Gamma$ A suppress ordering instabilities but strong long-range fluctuations persist and affect spectra and self-energies. An overview of the ABINITIOD $\Gamma$ A results and the evidenced momentum selectivity are presented in Sec. IV, before being analyzed in detail in Sec. V; implications will be discussed in Sec. VI. Finally, Sec. VII summarizes our conclusions.

## II. METHOD

The crystal structures used are identical to Ref. [28]: density function theory (DFT) calculations are based

on the WIEN2K package [58,59] with PBE [60] as exchange-correlation potential. We construct a slab as displayed in the insets of Fig. 1 consisting of one unit cell of SrVO<sub>3</sub> on top six unit cells of the SrTiO<sub>3</sub> substrate and surrounded (in  $z$  direction) by sufficient vacuum of about 10 Å to both sides. While the in-plane lattice constant of the heterostructure is locked to the (theoretical) SrTiO<sub>3</sub> substrate [61] ( $a_{\text{SrTiO}_3}^{\text{PBE}} = 3.95$  Å) all other internal atomic positions are relaxed, except for the two unit cells of SrTiO<sub>3</sub> furthest away from SrVO<sub>3</sub>. The WIEN2K band-structure is then projected onto maximally localized V- $t_{2g}$  Wannier orbitals, using the WIEN2WANNIER [62] interface to WANNIER90 [63]. The thus obtained Wannier Hamiltonian is supplemented by a Kanamori interaction using  $U = 5$  eV,  $J = 0.75$  eV,  $U' = 3.5$  eV and solved by dynamical mean-field theory (DMFT) [50,64]. Doping is modeled by a posterior-to-DFT adjustment of the chemical potential in DMFT. For DMFT spectral functions, analytic continuation was performed with the maximum entropy method implemented in ANA\_CONT [65]. There, the hyperparameter  $\alpha$  was determined with the CHI2KINK method and a preblur window size of  $\sigma = 0.05$  eV was employed.

In this paper, we go beyond DMFT [54,66] and treat nonlocal correlations in the SrVO<sub>3</sub> film with ABINITIOD $\Gamma$ A [53,67,68]. Contrary to finite-size cluster methods, the D $\Gamma$ A approach [51,52,54] and other, closely related diagrammatic extensions of DMFT [54,69–74] are not limited to short-range fluctuations. It well describes pseudogaps induced by antiferromagnetic fluctuations in the one-band 2D Hubbard model [12,75–81] and (quantum) critical behavior [2,82–84]. orbital ordering and ferromagnetic fluctuations have hitherto not been studied by D $\Gamma$ A or other diagrammatic extensions of DMFT. For the ABINITIOD $\Gamma$ A, we here calculate the local particle-hole irreducible vertex at DMFT self-consistency by continuous-time quantum Monte Carlo simulations in the hybridization expansion [85,86] using w2DYNAMICS [87] with worm sampling [88]. From this local vertex, we subsequently

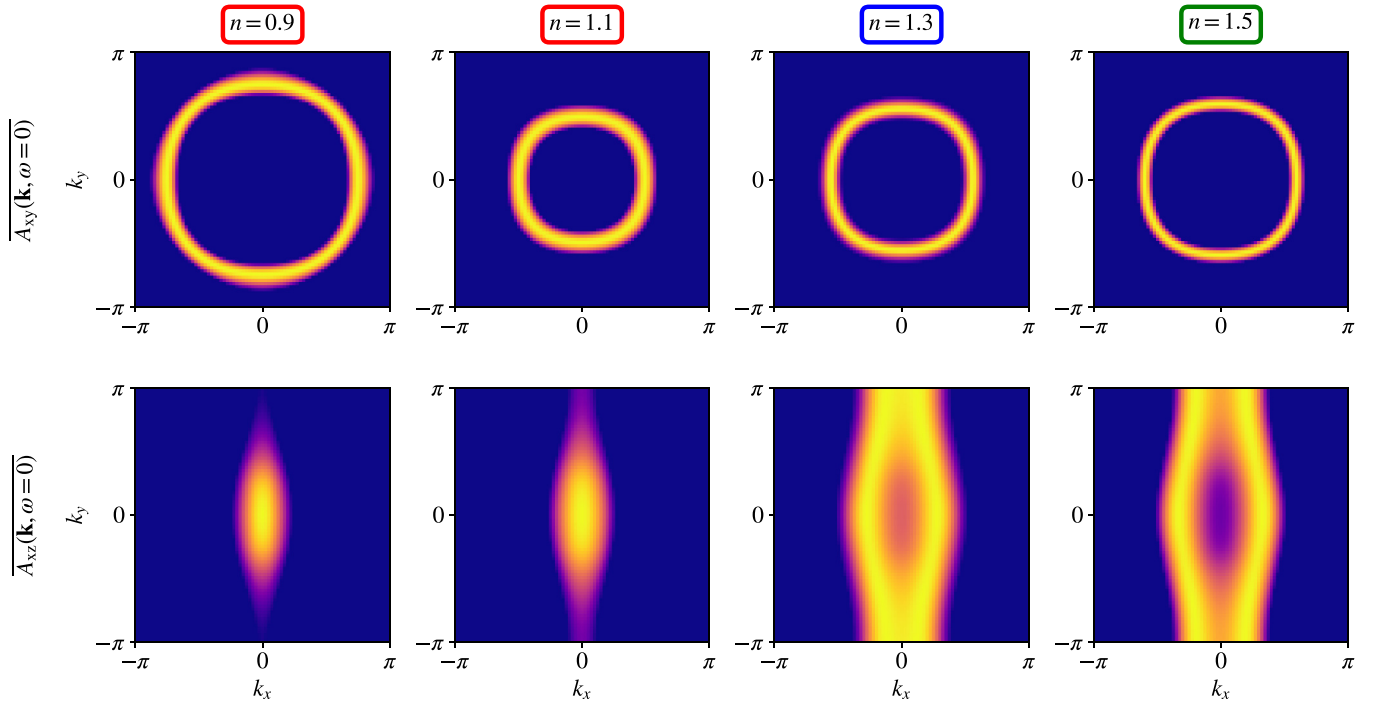


FIG. 2. SrO-terminated monolayer—DMFT Fermi surface for the points highlighted in Fig. 1(a):  $n = 0.9$  ( $T = 290$  K) and  $n = 1.1$  ( $T = 290$  K) order AF at low  $T$  (red box indicating the color code of Fig. 1), FM at  $n = 1.3$  ( $T = 190$  K; blue box), and cOO at  $n = 1.5$  ( $T = 230$  K; green box).

calculate the particle-hole and transversal particle-hole Bethe-Salpeter ladder diagrams, and, through the Schwinger-Dyson equation, the nonlocal self-energy. This way we include nonlocal correlation effects in the self-energy. The D $\Gamma$ A chemical potential was readjusted to fix the total number of electrons to the considered doping level. In this study we apply D $\Gamma$ A in a one-shot setting, forgoing nonlocal self-consistency [89]. For a review of the method, see Ref. [54]; for computational details of the ABINITOD $\Gamma$ A see Ref. [68]. D $\Gamma$ A and DMFT Fermi surfaces were obtained from the Green's function at imaginary time  $\tau = \beta/2$  ( $\beta = 1/k_B T$ ). This procedure corresponds to a spectral function  $A(\mathbf{k}, \omega = 0)$  that is averaged over a frequency interval  $\sim k_B T$  around the Fermi level. We note that our ABINITOD $\Gamma$ A calculations are not self-consistent. Therefore, the too large susceptibilities from DMFT, will lead to an overestimation of spectral renormalizations in D $\Gamma$ A. For a discussion of the relevance of the Mermin-Wagner theorem, see our preceding paper [28].

### III. DMFT: ORBITAL EFFECTS

The DMFT phase diagram Fig. 1 shows, as a function of doping and surface termination, a rich variety of different magnetic and orbitally ordered phases [28]. Nonlocal fluctuations will strongly suppress the DMFT phase transitions in quasi-two dimensions but lead, at the same time, to strong scattering rates and self-energy corrections. In Sec. IV, we will study these renormalizations using the D $\Gamma$ A at the  $(n, T)$  points indicated in Fig. 1. The temperatures have been chosen so that we are close to the respective phase transitions in DMFT and, thus, can expect pronounced nonlocal correla-

tions.<sup>1</sup> Before turning to these D $\Gamma$ A results, in this Section we first analyze the DMFT Fermi surfaces and  $\mathbf{k}$ -integrated spectra at the same fillings (orbitally resolved occupations, DMFT susceptibilities, and  $\mathbf{k}$ -integrated DMFT spectra at filling  $n = 1$  with and without crystal field splitting have already been presented in Ref. [28]). In DMFT, nonlocal fluctuations are not included and thus do not affect the self-energy and spectral function. As a consequence, approaching the ordered states does not result in a pronounced temperature dependence of the DMFT spectra and self-energy.

#### A. SrO termination

Figure 2 shows the DMFT Fermi surface for the SrO-terminated SrVO<sub>3</sub> monolayer at four different dopings (left to right). The upper panels display the contribution of the  $xy$  orbital and the lower panels the  $xz$  orbital (the  $yz$  orbital is equivalent to the latter if rotated by 90°).

We find the stoichiometric sample ( $n = 1$ ) to be an orbitally polarized insulator [44] with a gap of about 1 eV, see Fig. 3. That is, the in-plane  $xy$  orbital is essentially half-filled, while the  $xz, yz$  orbitals are almost completely depleted. Hence, the undoped SrO-terminated SrVO<sub>3</sub> monolayer is an effective one-orbital system. The reduced orbital-degeneracy (with respect to the bulks threefold  $t_{2g}$  orbitals) leads to a smaller critical interaction for the Mott state [90,91]. This

<sup>1</sup>Due to the multiorbital nature and the temperature scaling of the D $\Gamma$ A, we are restricted in temperature, i.e., we are not able to approach the FM instability much further.

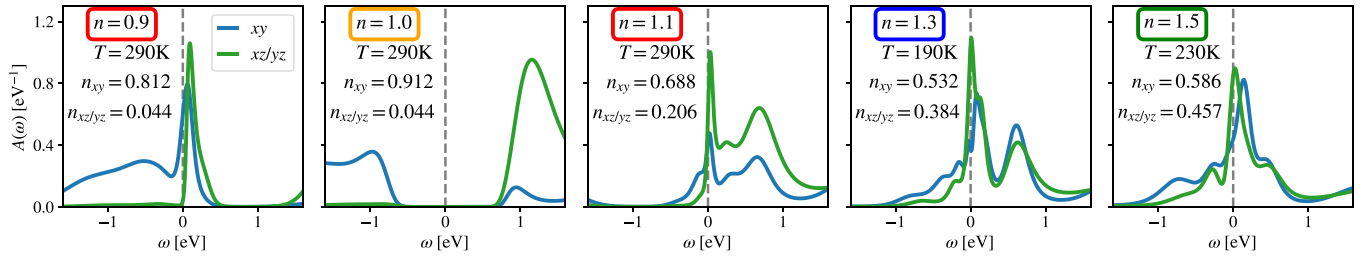


FIG. 3. SrO-terminated monolayer—DMFT spectral functions  $A(\omega)$  for various fillings  $n$  and temperatures  $T$ : in the Mott insulating state ( $n = 1.0$ ), in the vicinity of the AF ( $n = 0.9, 1.1$ ), FM ( $n = 1.3$ ), and cOO ( $n = 1.5$ ) phases, resolved into orbital characters ( $xy$  and  $xz/yz$ ). Colored boxes around fillings indicate the type of long-range orders realized at lower  $T$ , in correspondence to Fig. 1. At nominal filling ( $n = 1$ ; orange), an orbitally polarized Mott insulator forms [28,44].

turns the undoped SrVO<sub>3</sub> monolayer Mott insulating with strong antiferromagnetic (AF) fluctuations.

Doping with 10% electrons or holes, we obtain a metal, see the panels with  $n = 0.9$  and  $n = 1.1$ , respectively, in Refs. 2 and 3. The  $xz$  and  $yz$  orbitals are now slightly filled, pushing the AF phase transition to lower  $T$ , see Fig. 1, while strong AF spin fluctuations persist. The  $\mathbf{k}$ -integrated spectral function in Fig. 3 further shows that the  $xz$  and  $yz$  orbitals, while only slightly filled, already contribute a sizable amount to the quasiparticle peak at the Fermi level.

Similarities of this system to high- $T_c$  cuprates are uncanny. While, here, the low-energy physics is dominated by a half-filled  $xy$  orbital instead of the  $x^2 - y^2$  orbital in cuprates, we find a ratio of nearest to next-neighbor in-plane hopping  $t'/t = +0.31$ , ( $t = -0.237$  eV,  $t' = -0.073$  eV) which is essentially the same as found for YBa<sub>2</sub>Cu<sub>3</sub>O<sub>7</sub> and Bi<sub>2</sub>Sr<sub>2</sub>CaCu<sub>2</sub>O<sub>8</sub> [92], but  $t'$  has the opposite sign. In a one-band picture, one can compensate for the opposite sign by making a particle-hole transformation and we obtain an electronlike Fermi surface instead of a hole like one in cuprates. The decisive difference is however that, upon doping, the  $xz/yz$  orbitals become partially filled, leading to a different, multiorbital kind of physics.

Indeed, at larger doping,  $n = 1.5$ , Fig. 1 indicates a checkerboard orbital order (cOO) in DMFT with a spatially alternating occupation of the  $xz$  and  $yz$  orbitals, whereas the  $xy$  orbital does not participate in the cOO. Here, the  $xy$  and  $yz$  orbitals are already almost as much filled as the  $xy$  orbital as is evident from Fig. 3 and also from the Fermi surfaces in Fig. 2. As the  $xz$  ( $yz$ ) lobes point in the  $x$  ( $y$ ) and  $z$  directions, their Fermi surface in Fig. 2 is highly asymmetric, whereas their  $\mathbf{k}$ -integrated spectrum in Fig. 3 is similar to that of the  $xy$  orbital. In between, around  $n = 1.3$ , the  $xz$  and  $yz$  orbitals are still significantly less filled, however the spectral function at the Fermi level  $A(\omega = 0)$  is strongly enhanced, see Fig. 3. Ferromagnetic (FM) order therefore develops in Fig. 1 from the interplay of the Hund's coupling  $J$  and the hopping  $t$  [28,93].

### B. VO<sub>2</sub> termination

We now turn to the DMFT electronic structure of the VO<sub>2</sub>-terminated surface. Again, we show Fermi surfaces (Fig. 4) and  $\mathbf{k}$ -integrated spectra (Fig. 5) for varying doping. For the VO<sub>2</sub> instead of the SrO termination to the vacuum, the crystal-field splitting between the  $xz/yz$  and the  $xy$  orbital flips its sign [28]. That is, the  $xy$  orbital now lies above the  $xz/yz$  orbitals.

At  $n = 1$ , the latter accommodate all of the charge and their spectrum is split into upper and lower Hubbard bands, see Fig. 5, whereas the  $xy$  orbital is unoccupied. The two degenerate  $xz$  and  $yz$  orbitals are at or near quarter filling around  $n = 1$ . This gives rise to checkerboard orbital fluctuations and, at low enough temperature, ordering (cOO) in DMFT, see Fig. 1. For slight hole doping and substantial electron doping, the cOO tendencies remain intact, but the SrVO<sub>3</sub> layer turns metallic. Inverting the role of the  $xz/yz$  and the  $xy$  orbitals compared to the SrO-termination, we now observe a small hole pocket for the  $xy$  orbital in Fig. 4, in agreement with their small filling in Fig. 5.

Reducing the filling from  $n = 0.94$  to 0.85, this  $xy$  Fermi-surface pocket becomes slightly enhanced, albeit it remains small in Fig. 4. As for the fluctuations: because of their reduced filling, the  $xz/yz$  orbitals are no longer quarter-filled. Thus cOO gives way, first, to stripe orbital order (sOO) at  $n = 0.85$  and, eventually, at lower fillings to FM, similar as for the two-band Hubbard model [93].

Further electron doping from  $n = 1.23$  to 1.3 instead changes the DMFT ordered state from cOO to incommensurate magnetism (iM) with a small  $\mathbf{q}$  vector in Fig. 1, see Ref. [28]. It has, however, little effect on the spectral function and the Fermi surface in Figs. 4 and 5, respectively. The sharper Fermi surface for  $n = 1.3$  can be explained by the slight decrease in the temperature and the fact that *local* DMFT correlations get reduced the farther we are away from half-filling, see Fig. 9 below.

## IV. DΓA: MOMENTUM DIFFERENTIATION

On the dynamical mean-field level, many-body renormalizations are assumed to be isotropic (i.e., independent of momentum). In 3D, this is mostly a good approximation (see, however, Ref. [94]). Yet, when the effective dimensionality is reduced, as in our ultrathin film, renormalizations become increasingly nonlocal [29]. The major question we will answer here is: *To what extent do the nonlocal critical fluctuations—in the vicinity of the associated ordered states—lead to momentum-selective renormalizations?* To elucidate this question, we use the ABINITODΓA [53,67,68] methodology and scrutinize the electron self-energy  $\Sigma(\mathbf{k}, i\nu)$  in the vicinity of the DMFT ordering instabilities summarized above.



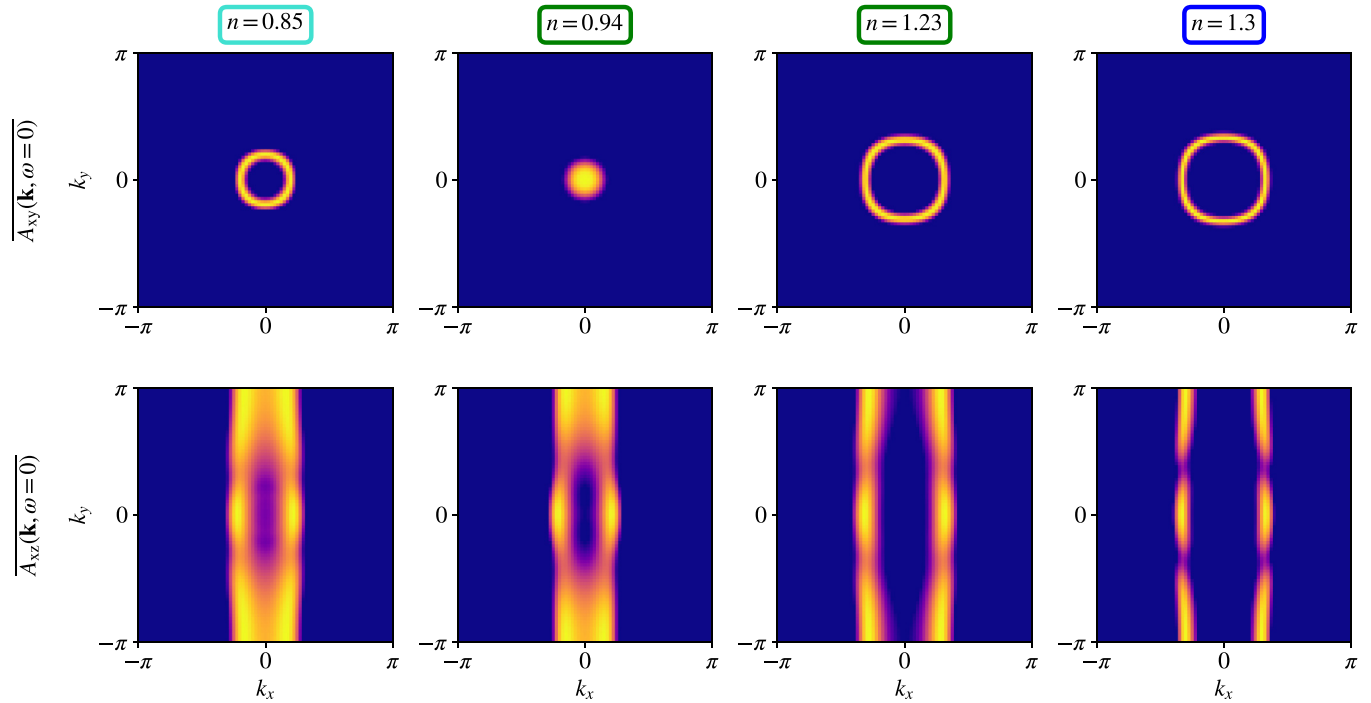


FIG. 4.  $\text{VO}_2$ -terminated monolayer—DMFT Fermi surface for the points highlighted in Fig. 1(b):  $n = 0.94$  ( $T = 290$  K) and  $n = 1.23$  ( $T = 290$  K) order cOO at low  $T$  (green box indicating the color code of Fig. 1),  $n = 0.85$  sOO ( $T = 210$  K; turquoise box), and  $n = 1.3$  iM ( $T = 190$  K; blue box).

### A. SrO termination

Figure 6 shows the real and imaginary parts of the ABINITIOD $\Gamma$ A self-energy in the vicinity of the DMFT phase transitions where nonlocal correlations become strong. Shown are the two inequivalent orbitals,  $xy$  (top) and  $xz$  (middle panel) as a function of Matsubara frequency  $\nu_n$ . The  $yz$  orbital is equivalent to the  $xz$  orbital if the momenta are rotated by  $90^\circ$  rotated; the DMFT self-energy is shown for comparison.

In the vicinity of half-filling,  $n = 0.9$  and  $1.1$ , AF spin fluctuations prevail with leading eigenvalue  $\lambda_M(\pi, \pi) = 0.95$  and  $0.79$ , respectively, in the magnetic ( $M$ ) channel at  $\mathbf{q} = (\pi, \pi)$ . Note,  $\lambda = 1$  indicates a divergence of the susceptibility, i.e., an ordering instability. These AF spin fluctuations are driven by the  $xy$  orbital that is close to half filling, whereas the  $xz$  and  $yz$  orbitals rather act as passive bystanders [28]. Consequently, we see for  $n = 0.9$  and  $n = 1.1$  in Fig. 6 a pronounced momentum differentiation only for the  $xy$  orbital.

The Matsubara frequency self-energy has the advantage that it does not require the ill-conditioned analytic continu-

ation. Nonetheless, we can gain valuable information: The momentum differentiation of the real part of the self-energy in Fig. 6 between unoccupied [ $\mathbf{k} = (\pi, \pi)$ , green] and occupied states [ $\mathbf{k} = (0, 0)$ , red] signals that the quasiparticle poles at  $\omega + \mu = \text{Re}\Sigma + \epsilon_{\mathbf{k}}$  are pushed further away from the Fermi energy, causing an overall *enhancement* of the bandwidth. The momentum differentiation between  $\mathbf{k} = (0, \pi)$  (blue) and  $\mathbf{k} = (\pi/2, \pi/2)$  (orange) that are closer to the Fermi level, indicates a deformation of the Fermi surface for  $n = 0.9$ , but not for  $n = 1.1$  which has a similar self-energy for these two  $\mathbf{k}$  points. Indeed, a deformation is observed in Fig. 7, where the electronlike DMFT Fermi surface (Fig. 2) turns into a holelike one in D $\Gamma$ A for  $n = 0.9$ . For  $n = 1.3$  with strong FM fluctuations [ $\lambda_M(0, 0) = 0.78$ ] and  $n = 1.5$  with strong cOO fluctuations in the density (D) channel [ $\lambda_D(\pi, \pi) = 0.98$ ], the momentum differentiation of  $\text{Re}\Sigma$  is less pronounced.

Let us now turn to  $\text{Im}\Sigma$  from which we can read off the scattering rate, as the  $\nu_n \rightarrow 0$ -extrapolated value. Further, from its slope the quasiparticle renormalization  $Z_{\mathbf{k}} = [1 - \partial \text{Im}\Sigma(\mathbf{k}, i\nu)/\partial \nu|_{\nu \rightarrow 0}]^{-1}$  is accessible for a Fermi

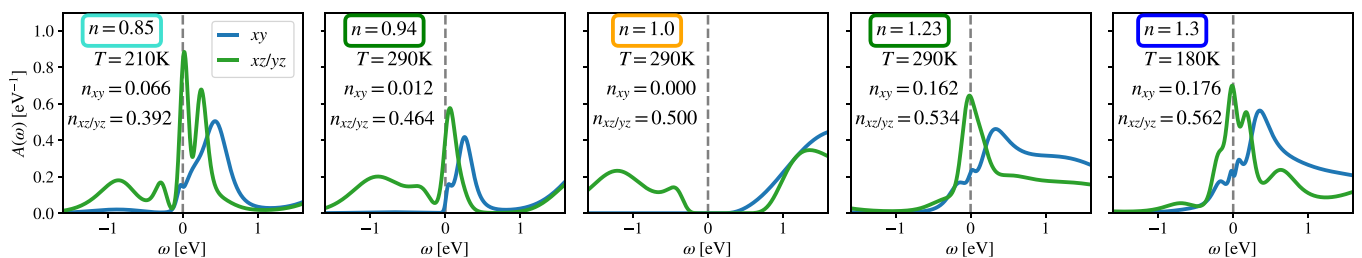


FIG. 5.  $\text{VO}_2$ -terminated monolayer—DMFT spectral functions  $A(\omega)$  for various fillings  $n$  and temperature  $T$ :  $n = 0.85$ : sOO;  $n = 0.94$ : cOO;  $n = 1.0$ : Mott insulating cOO;  $n = 1.23$ : cOO;  $n = 1.3$ : iM. Otherwise identical to Fig. 3.

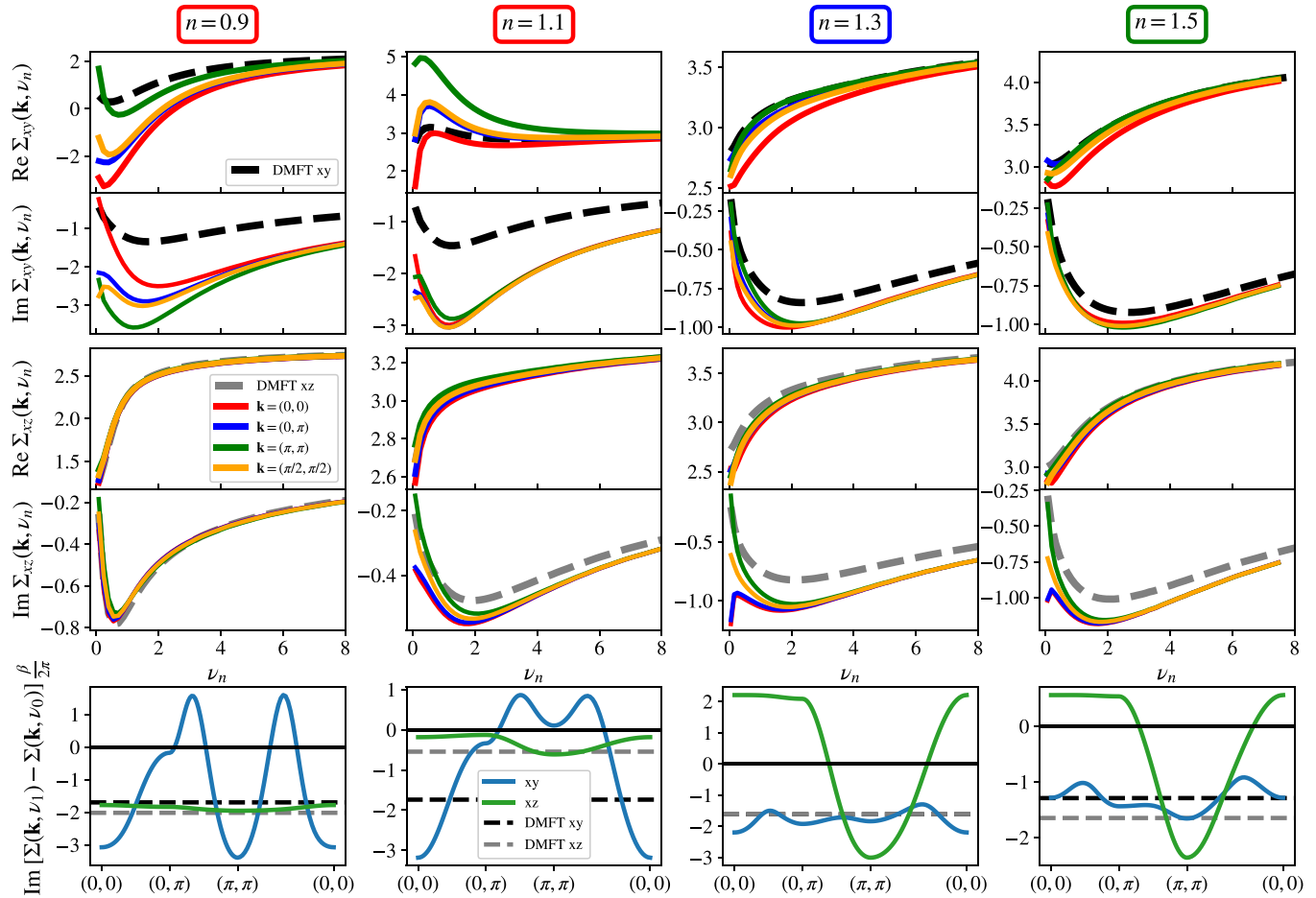


FIG. 6. SrO-terminated monolayer—momentum differentiation of the DΓA self-energy. (Top four rows) Real and imaginary parts for the  $xy$  and  $xz$  orbital at 4 different momenta, compared to DMFT, for the dopings and temperatures indicated in Fig. 1(a). (Bottom row) Slope of the imaginary part of the DΓA self-energy for a path through the Brillouin zone. Negative values correspond to a Fermi-liquid like self-energy, positive values indicate the formation of a (pseudo)gap.

liquid phase. A positive slope of  $\text{Im}\Sigma(i\nu \rightarrow 0)$  indicates the crossover to a diverging (Mott-like) self-energy, which splits the spectrum and leads to an insulating gap.

Clearly, for all four fillings shown in Fig. 6, there are momenta for which the system exhibits non-Fermi liquid behavior, identifiable by a kink and a downturn in  $\text{Im}\Sigma$  at low energies. In case of AF fluctuations ( $n = 0.9$  and  $1.1$ ) this downturn is in the  $xy$  orbital, whereas it occurs in the  $xz$  (and  $yz$ ) orbital which dominates the FM ( $n = 1.3$ ) and cOO ( $n = 1.5$ ) fluctuations. These kinks are salient indicators for the occurrence of a pseudogap state, and they get more pronounced when cooling the system toward the respective phase transition.

Interestingly, in the vicinity of the AF phase, the structure of the scattering rate is *opposite* to the cuprates: it is larger for the diagonal  $(\pi, \pi)$  direction than for the  $(0, \pi)$  direction. This momentum differentiation on the Fermi surface is, however, much less pronounced than the momentum dependence perpendicular to the Fermi surface, i.e., comparing occupied vs. unoccupied states.

This can be seen in Fig. 6 (bottom), where we plot the slope between the first two positive Matsubara frequencies, i.e., slope =  $(\text{Im}\Sigma(i\nu_1) - \text{Im}\Sigma(i\nu_0))\beta/(2\pi)$ , along the indicated  $\mathbf{k}$ -path. Isolines of this slope are superimposed on the DΓA

Fermi surfaces in Fig. 7, with the sign indicated by solid, fat (positive) and dashed, thin (negative) lines. In the electron doped regime, the slope in  $\text{Im}\Sigma$  is always negative on the Fermi surface, i.e., Fermi liquidlike. However, when moving away from the Fermi energy, we observe positive slopes, which corresponds to the kinks in Fig. 6: at  $n = 1.1$  for the unoccupied  $xy$  states above the Fermi level; and at  $n = 1.3$  and  $n = 1.5$  for the occupied  $xz$  states. In the hole doped regime, at  $n = 0.9$ , we find  $\text{Im}\Sigma$  isoline patterns similar to  $n = 1.1$ . However, owing to the larger  $xy$  occupation in combination with the equally strong reconstruction through  $\text{Re}\Sigma$ , negative slopes of  $\text{Im}\Sigma$  instead appear across the transformed  $xy$  Fermi surface. This insulatinglike behavior is found only in the most relevant orbitals, i.e., the  $xy$  orbital for the AF fluctuations around  $n = 1$ , and the  $xz/yz$  orbitals where FM and cOO long-range fluctuations are dominant. The ancillary orbitals ( $xz/yz$  for  $n = 1.1$  and  $xy$  for  $n = 1.3, 1.5$ ) on the other hand exhibit only a comparatively minor momentum differentiation (see Fig. 6)—implying also a stark orbital differentiation.

## B. VO<sub>2</sub> termination

The corresponding ABINITIODΓA results for the VO<sub>2</sub>-terminated SrVO<sub>3</sub> monolayer for the self-energy and the

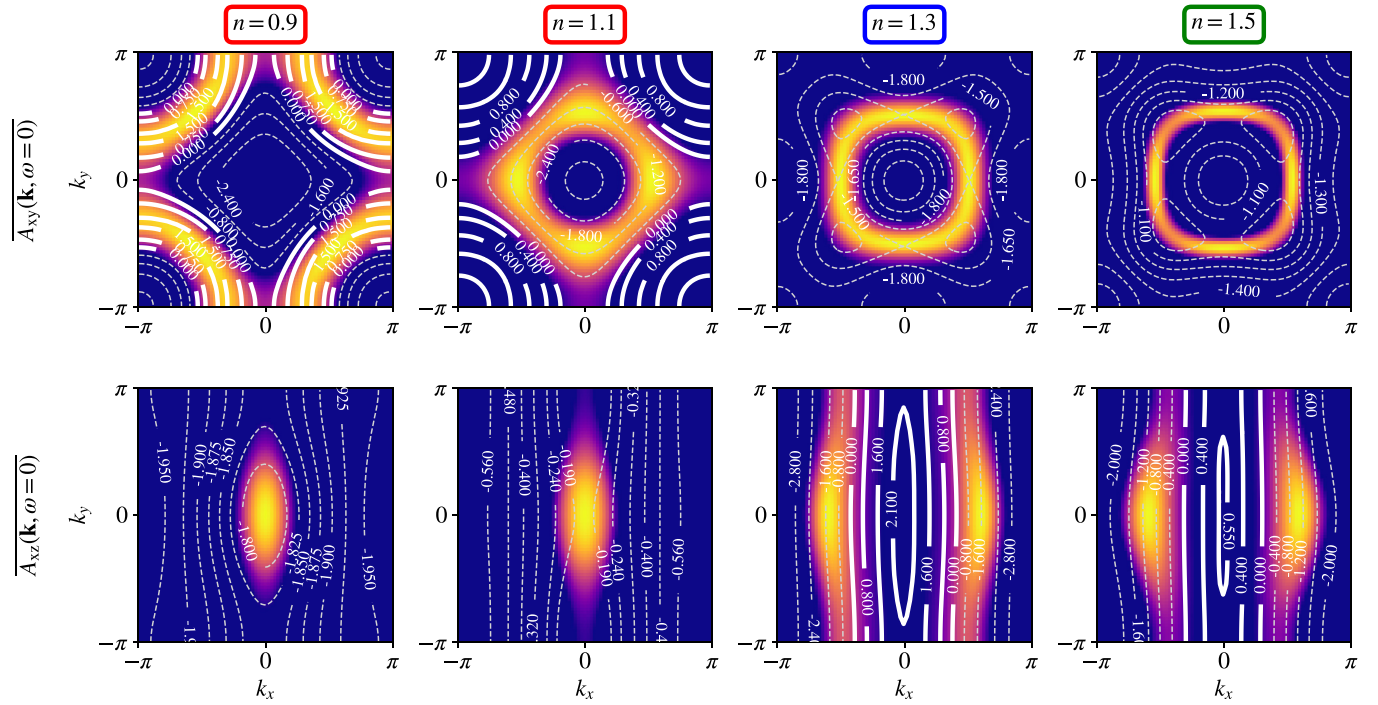


FIG. 7. SrO-terminated monolayer—Fermi surfaces at the same dopings and  $T$  as in Fig. 2. The white lines represent isolines of the slope between the first two Matsubara frequencies of the imaginary part of  $\Sigma$ : solid, fat lines indicate a *positive* slope, i.e., a kink in the self-energy, dashed, thin lines a *negative* value, suggestive of a Fermi-liquid-like state.

Fermi surface are presented in Figs. 8 and 9, respectively. For cOO fluctuations at  $n = 1.23$  ( $\lambda_D(\pi, \pi) = 0.97$ ), the momentum differentiation of the self-energy and Fermi surface are qualitatively similar to the cOO results at  $n = 1.5$  for the SrO-terminated layer. But for the cOO at  $n = 0.94$  and sOO at  $n = 0.85$ , we only find a minor momentum differentiation of the self-energy, see Fig. 8. Correspondingly, the Fermi surface in Fig. 9 is similar to that of DMFT in Fig. 4, and there are no positive non-Fermi-liquid like slopes (solid lines in Fig. 9). This is surprising since the leading eigenvalue  $\lambda_D(0, \pi) = \lambda_D(\pi, 0) = 0.985$  at  $n = 0.85$  and  $\lambda_D(\pi, \pi) = 0.91$  at  $n = 0.94$  is similarly close to 1 as for  $n = 1.23$  or the SrO termination, indicating that strong orbital ordering fluctuations are present.

On the contrary, at  $n = 1.3$ , above iM order, we observe the by far strongest momentum differentiation in Fig. 8, even though  $\lambda_M(\delta, \delta) = 0.97$  with  $\delta \approx \pm\pi/4$  is again comparable to the strength of other fluctuations. A clear pole develops in the vicinity of the Fermi level not only for the  $xz$  and  $yz$  orbitals, that drive the iM ordering, but also for the  $xy$  orbital. This pole is so large that the spectrum splits into two parts, akin to the splitting into upper and lower Hubbard band; and it pushes the Fermi surface to  $\mathbf{k} = (0, \pm\pi)$ . However, the divergence occurs only for a region of the Brillouin zone that does not account for the Fermi surface of the respective orbital character.

## V. BINAURAL FLUCTUATION DIAGNOSTICS

We now expose the connection between strong nonlocal two-particle fluctuations and the occurrence (or not) of large, momentum-selective corrections to one-particle spectral

properties. To this end, we revisit the ABINITIOD $\Gamma$ A equation of motion [53]: the self-energy of spin  $\sigma$  consists of the Hartree-Fock (“HF”) contribution and a term that includes all truly two-particle scattering events by linking the density vertex  $F_D$  with the interaction matrix  $U$ , the bare susceptibility  $\chi_0$ , and a Green’s function  $G$  that closes the Feynman diagram

$$\Sigma_{\sigma}^k = \Sigma_{\sigma}^{\text{HF}} - \frac{1}{\beta} \sum_{\substack{qk' \\ lhn, rst}} U_{mlhn} \chi_{0, nlsr}^{qk'k'} F_{rstm'}^{qk'k} G_{\sigma}^{k-q}. \quad (1)$$

In this notation,  $q, k, k'$  refer to compound indices consisting of pairs of momenta and Matsubara frequencies,  $(\mathbf{q}, i\omega)$ ,  $(\mathbf{k}, iv)$ ,  $(\mathbf{k}', iv')$ . In the ladder approximation employed in ABINITIOD $\Gamma$ A,  $F_D$  is constructed from the Bethe-Salpeter equations in the particle-hole (“ph”) channel with an additional enforcement of crossing symmetry via the parquet equation [52,53]. The resulting expression

$$F_{lmm'l'}^{qkk'} = F_{lmm'l'}^{\omega vv'} + F_{lmm'l'}^{qv v', nl} + \frac{1}{2} F_{lmm'l'}^{(k'-k)(v'-\omega)v', nl} - \frac{3}{2} F_{lmm'l'}^{(k'-k)(v'-\omega)v', nl} \quad (2)$$

contains both charge (density, “ $D$ ”) and spin (magnetic, “ $M$ ”) fluctuations. The nonlocal (nl) particle-hole ( $ph$ ) vertices are calculated through the Bethe-Salpeter equation, and a local contribution with only frequency and orbital dependencies is subtracted to avoid a double counting. We can further decompose Eq. (1) into the DMFT self-energy and nonlocal corrections to it,

$$\Sigma_{\sigma}^k = \Sigma_{\sigma}^{v, \text{DMFT}} + \Sigma_{\sigma}^{k, \text{correction}} \quad (3)$$

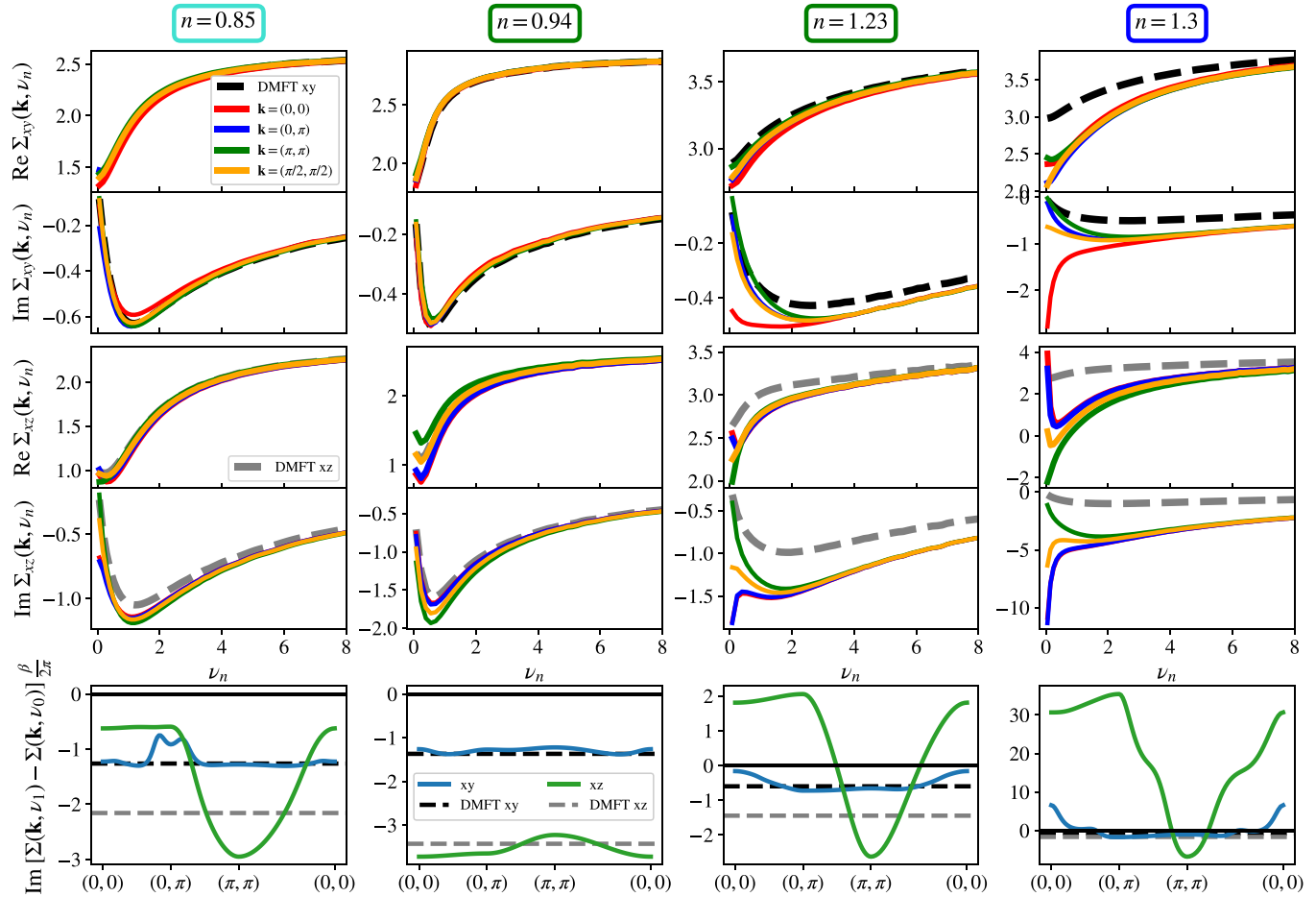


FIG. 8.  $\text{VO}_2$ -terminated monolayer—momentum differentiation of the DGA self-energy. (Top four rows) Real and imaginary parts for the  $xy$  and  $xz$  orbital for four different momenta (colors) and, for comparison, the DMFT self-energy (dashed) at the four dopings and  $T$  indicated by the “+” in Fig. 1(b). (Bottom row) Slope of the imaginary part of the DGA self-energy for a momentum path through the Brillouin zone.

as the purely local vertex of Eq. (2) combines with the Hartree-Fock contribution of Eq. (1) to the DMFT self-energy. The correction term,  $\Sigma^{k,\text{correction}}$ , then contains all nonlocal contributions and is efficiently implemented as a linear combination of various three-leg vertices, see Ref. [68]. For our purpose, we now transform internal momenta and frequencies in the corrections to DMFT by substituting  $k'' = k - q$ , leading to

$$\Sigma_{mm'}^{k,\text{correction}} = \Sigma_{mm'}^{\text{HF}} - \Sigma_{mm'}^{\nu,\text{DMFT}} + \sum_{k''} \Xi_{mm'}(k, k''), \quad (4)$$

where we lumped all internal summations except that over  $k''$  into

$$\Xi_{mm'}(k, k'') = -\frac{1}{\beta} \sum_{lhn,rst} U_{mlhn} \chi_{0,nlsr}^{(k''-k)k'} F_{rstm'}^{(k''-k),k'} G_{ht}^{k''}. \quad (5)$$

Now, by selecting a specific momentum  $k$  of the self-energy correction,  $\Sigma^{k,\text{correction}}$ , we are able to identify the contributions stemming from momentum  $k''$  via  $\Xi(k, k'')$ . This analysis allows highlighting the link between the electronic structure (encoded in  $G^{k''}$ ) and nonlocal fluctuations (included in  $F$ ): in the vicinity of spontaneous instabilities,  $F_D$  will peak at zero (bosonic) energy transfer,  $i\omega = i(\nu'' - \nu) =$

0, while the characteristic momentum transfer  $\mathbf{Q} = \mathbf{k}'' - \mathbf{k}$  depends on the dominant type of fluctuations. Since we are interested in renormalizations at low energies, we limit the discussion to the lowest fermionic Matsubara frequency,  $\nu = \nu_0 = \pi/\beta$ , implying also  $\nu'' = \pi/\beta$ . Focusing then on the momentum dependence,

$$\Xi_{mm'}(\mathbf{k}, \mathbf{k}'') \equiv \Xi_{mm'}((\mathbf{k}, i\nu_0), (\mathbf{k}'', i\nu_0'')), \quad (6)$$

we note that (in the absence of nesting) the bare susceptibility  $\chi_0$  contributes only minimally to the  $\mathbf{k}$  dependence. The momentum structure is, hence, dominantly generated from the interplay of the vertex  $F_D^{(k''-k)}$  and the Greens function  $G^{k''}$ . We find a strong momentum variation in the *imaginary* part of the self-energy correction to originate from the *real* part of the vertex and the *imaginary* part of the Green’s function. The latter is a direct reflection of the underlying Fermi surface, while the vertex’s amplitude is driven by the dominant fluctuations.

Essentially, large corrections to electronic lifetimes will be generated at Brillouin zone momenta  $\mathbf{k}$  if they can be connected to a Fermi surface via the transfer momentum  $\mathbf{Q}$  of the existing fluctuations. This connection does not need to be precise. First, deviations in the transfer momentum that are within the bounds of the (inverse) correlation length,  $\xi^{-1}$ ,



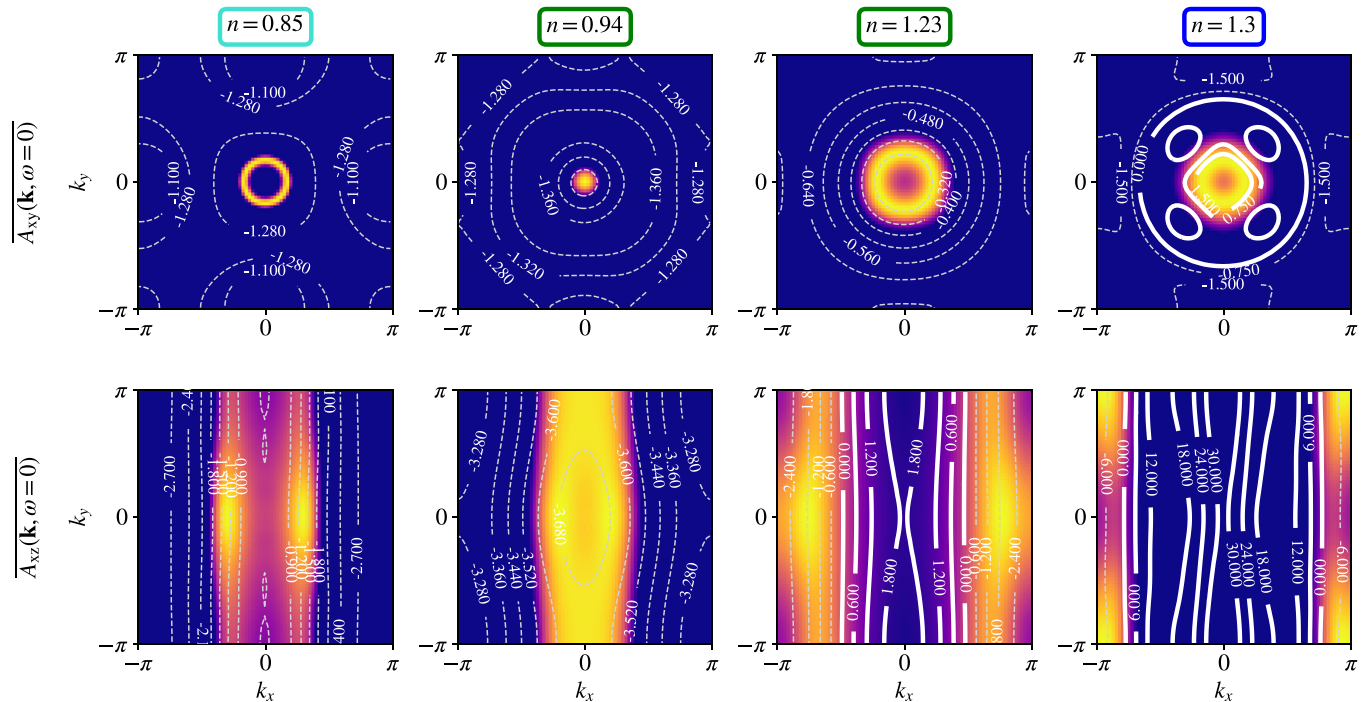


FIG. 9.  $\text{VO}_2$ -terminated monolayer—DFA Fermi surfaces at the same dopings and  $T$  as in Fig. 4. Isolines are again the low-energy slope of  $\text{Im}\Sigma$ , where the solid, fat lines represent a positive, and the dashed, thin lines represent a negative value.

will still produce a large signature in  $\Xi$  [22]. Second, the (DMFT) scattering rate  $\Gamma = Z\text{Im}\Sigma(\omega = 0)$  allows excitations to contribute even if they are at a distance  $\mathcal{O}(\Gamma/2)$  away from the Fermi surface.

Our decomposition of the equation of motion derives from previous approaches for the diagnostics of fluctuations [79,95,96]. Our contribution to the diagnostics tool box is twofold. First, we supplemented the fluctuation diagnostics with a second layer of analysis. We plot the fluctuation diagnostics together with the Fermi surface, providing a link between the dominant fluctuation momentum  $\mathbf{Q}$  and spectral properties at  $\mathbf{k}''$  for the studied momentum  $\mathbf{k}$ , see Fig. 10 and the animations in Ref. [97]. This additional layer helps explaining when and why nonlocal renormalizations from particular fluctuations become large. We call this doubled-down analysis that pairs fluctuation diagnostics with spectral information: “binaural fluctuation diagnostics.”<sup>2</sup> Second, we extended the domain of the fluctuation diagnostics from many-body models to realistic multiorbital materials.

Using the above “binaural fluctuation diagnostics,” we now analyze the self-energy corrections shown in the left column of Fig. 10 for both surface terminations, various doping levels, hosting orbitals, and  $\mathbf{k}$ -points. The positions of three selected  $\mathbf{k}$  points are indicated in the Brillouin zone plots in the three adjacent columns. There, the colored heat maps (blue: negative, red: positive, white: no correction) illustrate  $\text{Im}\Xi_{mm}(\mathbf{k}, \mathbf{k}'')$  from Eq. (6). The grey shaded overlay

corresponds to the Fermi surface of the selected orbital  $m$ . See Ref. [97] for an animated version of Fig. 10.

In close proximity to the antiferromagnetic DMFT phase transition (SrO termination;  $n = 1.1$ ; top row), the momenta  $\mathbf{k}_1$  and  $\mathbf{k}_2$  display a pronounced kink in the correction to the  $xy$  self-energy. Our momentum diagnostics reveals that these momenta can indeed be connected to the  $xy$  Fermi surface via the AF ordering vector  $\mathbf{Q} = (\pi, \pi)$ , generating a large amplitude in  $\text{Im}\Xi(\mathbf{k}_{1,2}, \mathbf{k}_{1,2} - \mathbf{Q})$ . Due to the shape and size of the Fermi surface, momenta—for which this constructive interplay with the AF fluctuations is possible—naturally lie in *unoccupied* regions of the Brillouin zone. Instead, *occupied* momenta, such as  $\mathbf{k}_3$ , cannot be connected to the Fermi surface via the AF ordering vector. As a result, there is no kink in  $\mathbf{k}_3$ 's self-energy correction and the overall shape is Fermi liquidlike. This insight into the momentum-structure of the equation of motion thus explains the evidenced momentum asymmetry ( $k_x > k_F$ ) in the scattering rate. While corrections at  $\mathbf{k}_3$  are small compared to those at  $\mathbf{k}_1$  and  $\mathbf{k}_2$ ,  $-\text{Im}\Sigma_{xy}^{\mathbf{k}_3, \text{correction}}(i\nu \rightarrow 0) \sim \mathcal{O}(0.5)$  eV is still larger than some of the corrections at other dopings, discussed below. The reason is the large (DMFT) scattering rate,  $-\text{Im}\Sigma_{xy}^{\nu=\pi/\beta, \text{DMFT}} \approx 0.7$  eV, see Fig. 6: it causes incoherent spectral weight of bands slightly below  $E_F$  (cf. Fig. 2(a) in Ref. [28]) to spill to the Fermi level, thus contributing to  $\Xi(\Gamma, M)$ .

Larger electron doping at  $n = 1.3$  favors ferromagnetism hosted by the  $xz/yz$  orbitals (second row in Fig. 10). Here  $\mathbf{Q} = (0, 0)$  (hence no arrow) naturally causes corrections to appear at the occupied states within the Fermi surface because it is rather narrow. The extent of the momentum region in which the FM-driven  $\Xi$  is large (see the diameter of the (blue) circular region) owes to the inverse correlation length  $\xi^{-1}$  that was found to be sizably larger than for dominant fluctuations

<sup>2</sup>Without the connection to fluctuation diagnostics, related momenta and Fermi surface analyses have been done before, e.g., in Ref. [22].

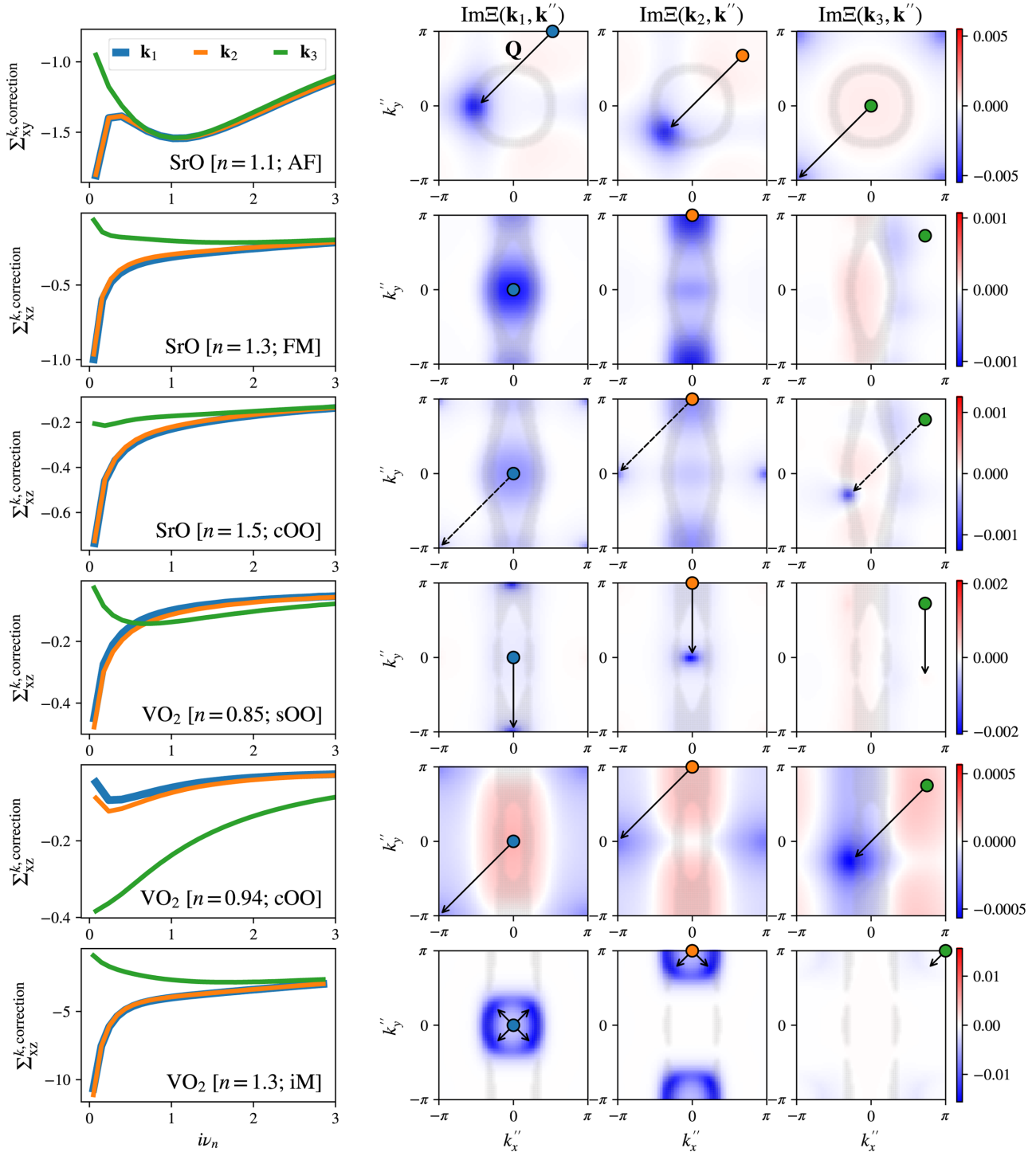


FIG. 10. Binaural fluctuation diagnostics. (Left) Self-energy correction to  $\Sigma_{\text{DMFT}}$  for six selected terminations, fillings,  $k$  points, and orbitals. (Right) Binaural fluctuation diagnostics for these six cases, consisting of (i) the corresponding momentum ( $k''$ ) fluctuation diagnostics  $\text{Im}\Xi(\mathbf{k}, \mathbf{k}'')$  from Eq. (6) at the first positive fermionic and zeroth bosonic Matsubara frequency (three columns on the right). (ii) Marking the selected  $\mathbf{k}$  points ( $\mathbf{k}_1, \mathbf{k}_2, \mathbf{k}_3$ ) in the Brillouin zone plots as colored circles, indicating the dominant wave vector  $\mathbf{Q}$  (arrows) of a given type of fluctuations, and the Fermi surface (gray shaded area) of the same orbital. Strong corrections are a product of strong fluctuations (large  $F_D^Q$ ) where the momentum transfer  $\mathbf{Q}$  (arrows) connects the self-energy momentum  $\mathbf{k}$  to the Fermi surface (gray shaded area) of the same orbital. While antiferromagnetic fluctuations cause strong corrections at momenta *outside* the Fermi surface (top row), ferromagnetism and the observed incommensurate magnetism are prone to corrections *inside* the Fermi surface (second and last row). Orbital ordering on the other hand is different (third and fifth row): checkerboard fluctuations have little to no effect, while stripe ordering promotes moderate corrections. This analysis reveals that in the SrO-terminated structure at  $n = 1.5$  (third row) the adjacent ferromagnetism is the root cause of the sizable renormalization, not the orbital order fluctuations that dominate the susceptibility. For animations with more  $\mathbf{k}$  points, see Ref. [97].

at other dopings, see Fig. 6(c) in Ref. [28] for a comparison. The large  $\xi^{-1}$  enables the  $\Gamma$  point, which manifestly is not on the Fermi surface, to significantly contribute to the self-energy corrections. Instead,  $\mathbf{k}_3$  is far enough from the Fermi surface for corrections to be suppressed.

Doping further to  $n = 1.5$ , the  $xz/yz$  orbitals become close to quarter-filling and a checkerboard orbital ordering instability emerges (third row in Fig. 10). Interestingly, the corresponding characteristic vector  $\mathbf{Q} = (\pi, \pi)$  of the cOO fluctuations, only plays a minor role in the lifetime differentiation: for  $\mathbf{k}_1$  and  $\mathbf{k}_2$ ,  $(\pi, \pi)$  connects to a small region of finite intensity in  $\Xi$  far away from the Fermi surface. However, larger contributions to the self-energy correction manifestly still come from the high amplitude around  $\mathbf{Q} = (0, 0)$ , i.e., from the direct vicinity of the  $\mathbf{k}_1$  and  $\mathbf{k}_2$  momenta in Fig. 10: spectral renormalizations are dominated by FM fluctuations although, at the current doping level, these are subleading in the susceptibility. This interpretation is further supported by looking at  $\mathbf{k}_3$ , where FM contributions are absent. There, self-energy corrections from  $(\pi, \pi)$  fluctuations are largest, as this momentum transfer directly connects  $\mathbf{k}_3$  to the Fermi surface. However, the resulting corrections are nonetheless very small. One contributing factor is again the inverse correlation length,  $\xi^{-1}$ . It is smaller for cOO than for FM by one order of magnitude (cf. Fig. 6(c) in Ref. [28]), resulting in a smaller ( $k_x'', k_y''$ ) region with finite (blue) intensity to integrate over. We can motivate an additional factor: The OO susceptibility of two orbitals  $l \neq m$  can be expanded into a linear combination of the density susceptibilities in which diagonal and off-diagonal components enter with *opposite* sign

$$\chi_{OO}^{lm} = 2\chi_D^{llll} + 2\chi_D^{mmmm} - 4\chi_D^{llmm}. \quad (7)$$

The entering diagonal and off-diagonal  $\chi_D^{llmm}$  for  $l, m \in \{xz, yz\}$  are displayed Fig. 11(b). While  $\chi_{OO}^{lm}$  for fixed  $l \neq m$  is naturally large in an OO regime, we empirically find the density susceptibility,  $\chi_D = 2 \sum_{lm} \chi_D^{llmm}$ , in which the above terms are summed with the *same* (plus) sign, to be small, see Fig. 11(d), suggestive of compensational effects. Similar to  $\chi^D$ , also the equation of motion involves a summation over diagonal and off-diagonal components, this time of  $F$ :

$$\begin{aligned} \sum_{\sigma}^{k_{mm}} \propto \sum_{qk'} U \left( \chi_{0,mmmm}^{qk'k'} F_{mmmm}^{qk'k'} + \chi_{0,llll}^{qk'k'} F_{llmm}^{qk'k'} \right) G_{\sigma}^{k-q} \\ + \mathcal{O}(J), \end{aligned} \quad (8)$$

where we omitted terms involving the Hund's coupling  $J$  and restricted  $G$  and  $\chi_0$  to diagonal elements,  $G_{mm}$  and  $\chi_{0,lmml}$ , mostly warranted in the systems considered here. Large off-diagonal contributions are only expected where bands hybridize, e.g., where the  $xz$  and  $yz$  orbitals cross. The observation made for  $\chi^D$  then suggests that also the orbital summation in the equation of motion results in an (at least partial) cancellation of terms headed by  $U$ . Quite intuitively for orbital fluctuations, leading corrections will then be driven by a smaller energy scale: the Hund's coupling  $J$ . These intricacies highlight that strong nonlocal fluctuations do not always translate 1-to-1 into large nonlocal renormalizations in spectral properties.

Similar arguments hold for the cOO regime at filling  $n = 0.94$  for the film with  $\text{VO}_2$  termination (fifths panel in Fig. 10).

Additionally, there is a modulation in the  $\mathbf{k}''$  plane, with positive contributions compensating part of the self-energy enhancement from around  $\mathbf{k} + \mathbf{Q}$ .

The argument of compensations in  $F_D$  does not hold for stripe orbital ordering for filling  $n = 0.85$  and  $\text{VO}_2$  termination (fourth panel in Fig. 10). Similar to the ferromagnetic case, the  $\mathbf{Q} = (0, \pi)$  nematic fluctuation vector supports a strong differentiation between occupied ( $\mathbf{k}_1, \mathbf{k}_2$ ) and unoccupied states ( $\mathbf{k}_3$ ) in the  $xz$  orbital. We speculate that the lower symmetry of the sOO state obviates cancellation effects in the equation of motion. Indeed, compared to the cOO regime, the sOO orbital-summed density susceptibility,  $\chi^D$ , and the partial sum  $\chi_D^{xz,xz} + \chi_D^{xz,yz}$  that mirrors the orbital combinations entering the equation of motion, Eq. (8), is one order of magnitude larger, cf. Figs. 11(c) and 11(d).<sup>3</sup>

Lastly, the incommensurate nature of the magnetic ordering at  $n = 1.3$  in the  $\text{VO}_2$ -terminated structure is easily seen as the root cause of the massive self-energy corrections in the last row of Fig. 10: the  $\mathbf{Q} = \delta \times \hat{\mathbf{e}}_Q$  vector is able to perfectly connect onto the Fermi surface for  $k_x'' = 0$ . Due to the large  $\delta \sim \pi/4$  also most other  $\mathbf{k}$  points are able to—at least partially—connect onto the Fermi surface—with zone-boundary momenta, such as  $\mathbf{k}_3$ , being the only exceptions. The momentum diagnostics hence provides an explanation for the wide range of positive slopes in  $\text{Im}\Sigma(i\nu)$  throughout the Brillouin zone, shown in Fig. 9. Incidentally, the onset of this magnetism is also the main driver of the corrections at slightly smaller doping  $n = 1.23$  where, yet again, the cOO fails to contribute. Consequently both the D $\Gamma$ A Fermi surfaces and low-energy slopes of  $\text{Im}\Sigma$  are qualitatively identical for  $n = 1.23$  and  $1.3$  in Fig. 9.

In all, we find that all types of *spin* fluctuations provide a path to strong nonlocal renormalizations. Our analysis further motivates the asymmetry with respect to the Fermi surface to be a direct consequence of the interplay of shape and size of the Fermi surface and the ordering vector  $\mathbf{Q}$  of the driving fluctuations.<sup>4</sup> The impact of *orbital* fluctuations, instead, is more ambiguous. Our work suggests that checkerboard orbital fluctuations only produce a weak momentum differentiation in the self-energy, while stripe-orbital fluctuations have larger signatures. A simpler model should be studied to further elucidate spectral consequences of orbital fluctuations in the absence of other complications.

## VI. DISCUSSION AND PERSPECTIVE

Recapitulating, we have studied a  $\text{SrVO}_3$  monolayer on a  $\text{SrTiO}_3$  substrate with two different surface terminations,  $\text{SrO}$  and  $\text{VO}_2$ , to vacuum within ABINITI $\Gamma$ A. Depending on the termination and filling, there are strong nonlocal fluc-

<sup>3</sup>Note also that the sOO data point is much closer to its DMFT ordering temperature than the cOO one (eigenvalues:  $\lambda_{sOO} = 0.985 > \lambda_{cOO} = 0.91$ ), suggestive of overall larger fluctuations.

<sup>4</sup>In a related analysis of the 2D doped Hubbard model [22], it was shown that an interplay of Fermi surface shape, van-Hove singularities and the coherence length of the antiferromagnetic fluctuations can further lead to a self-energy differentiation *on* the Fermi surface [22].

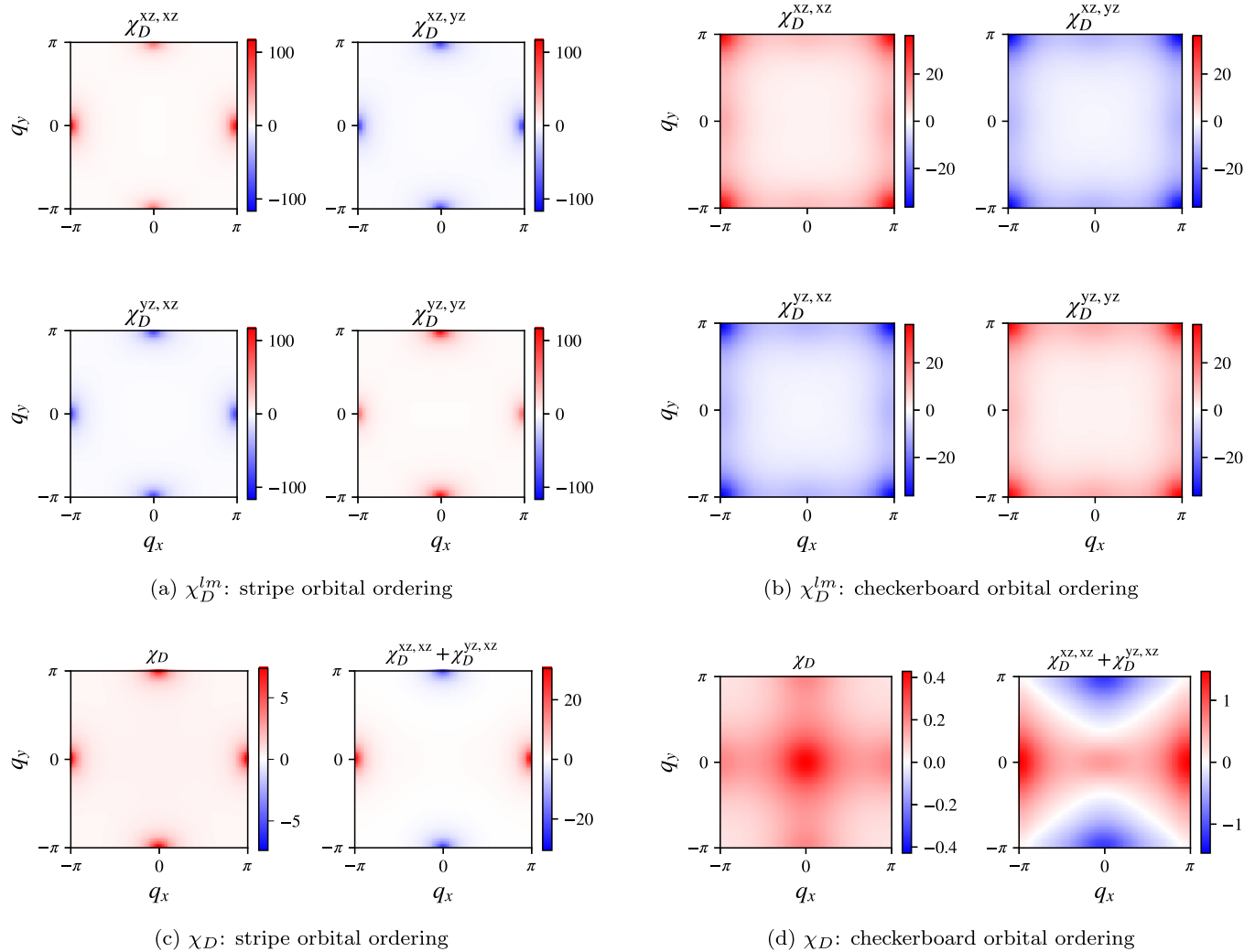


FIG. 11. Density susceptibilities in the  $(q_x, q_y)$  plane. [(a) and (b)]  $\chi_D$  matrix in the  $xz/yz$ -orbital space and the vicinity of stripe orbital ordering and checkerboard orbital ordering found in the  $\text{VO}_2$  terminated monolayer at  $n = 0.85$  and  $0.94$ , respectively. The sOO response in (a) displays orbital asymmetry where  $\chi_D^{xz,xz}(\pi, 0) > \chi_D^{xz,xz}(0, \pi)$  and vice versa for the  $yz$  orbital. The cOO response in (b) on the other hand is perfectly symmetric, i.e.,  $\chi_D^{xz,xz}(\pi, \pi) = \chi_D^{yz,yz}(\pi, \pi) = -\chi_D^{xz,yz}(\pi, \pi) = -\chi_D^{yz,xz}(\pi, \pi)$ . [(c) and (d)] Orbital-summed density susceptibility  $\chi_D = 2 \sum_{lm} \chi_D^{lm}$  and the nonsymmetric sum  $\chi_D^{xz,xz} + \chi_D^{yz,xz}$  motivated by Eq. (8). The aforementioned asymmetry manifests itself in a—for sOO fluctuations—large remainder in  $\chi_D^{xz,xz} + \chi_D^{yz,xz}$ , which is strongly attenuated in the vicinity of the cOO phase (note the different color scales).

tuations of various kinds: antiferromagnetic, ferromagnetic, incommensurate magnetic, striped or checkerboard orbital. These nonlocal fluctuations will suppress the mean-field DMFT ordering but also have pronounced effects on the self-energy—the focus of the present paper. They can deform the Fermi surface, as observed for antiferromagnetic ordering with  $n = 0.9$  for SrO-terminated  $\text{SrVO}_3$ , and quite generally can lead to a strong enhancement of  $\text{Im}\Sigma$ . Strong nonlocal fluctuations can even cause the development of a pole in the self-energy, signaling the splitting of the spectrum into two parts—here not because of Mott-Hubbard physics but because of large nonlocal fluctuations. The latter is particularly strong for the incommensurate ferromagnetic phase of the  $\text{VO}_2$ -terminated  $\text{SrVO}_3$  monolayer at  $n = 1.3$  filling. First indications, i.e., downturns of the self-energy at the lowest Matsubara frequency are however ubiquitous for various dopings and both terminations. While such nonlocal physics have

been investigated quite intensively for antiferromagnetic fluctuations in the Hubbard model in the context of the cuprates, to the best of our knowledge it has not been analyzed before for orbital fluctuations.

The undoped ( $n = 1$ )  $\text{SrVO}_3$  monolayer is Mott insulating and, for SrO-termination, appears to be akin to the cuprates with the  $xy$  orbital playing the role of the high- $T_c$ 's  $x^2 - y^2$  orbital. However, electron-doping reveals the multiorbital physics of the  $\text{SrVO}_3$  system: The  $xy$  orbital is depopulated when adding electrons to the system, and all three orbitals,  $xy$ ,  $xz$ , and  $yz$ , participate in developing a quasiparticle resonance at the Fermi level.

For the cuprates, AF fluctuations lead to pseudogap physics with a momentum differentiation distinguishing between a Fermi liquidlike self-energy in the nodal direction on the Fermi surface, and a kink in the self-energy signaling the opening of a gap in the antinodal direction. Here, we also



observe the joint presence of these two behaviors in the self-energy. However, the momentum differentiation is not realized *on* the Fermi surface but *perpendicular* to it: for the SrO-termination in the electron-doped regime, AF fluctuations lead to a Fermi liquidlike behavior for momenta on the occupied side of the Fermi surface (“ $k < k_F$ ”) and a kinklike insulating behavior in the imaginary part of the self-energy on the unoccupied side (“ $k > k_F$ ”). In case of FM fluctuations, the momentum differentiation between occupied and unoccupied momenta is reversed. The tendency towards checkerboard orbital ordering, however, has no vital influence on the self-energy.

For the VO<sub>2</sub> termination, iM fluctuations at  $n = 1.3$  lead to massive nonlocal correlations and a pole in the self-energy. In contrast to all other cases not only the  $xz/yz$  orbitals—driving the iM fluctuations—are affected but also the ancillary  $xy$  orbital. Around half-filling, again, the cOO fails to contribute significantly to the self-energy. Instead, sOO fluctuations do generate a momentum differentiation.

The imaginary part of the self-energy corresponds to the lifetimes and the broadening of the spectral function. Our results hence show that the lifetimes of an added hole or electron are extremely different. The hole lifetime can be measured by angular resolved photoemission spectroscopy (ARPES); the electron lifetime by inverse photoemission spectroscopy, by ARPES at elevated temperatures, or in nonequilibrium situations (e.g., pump-probe measurements) in which states above the Fermi level become populated.

The differentiation between states above and below the Fermi surface that we observe is quite extreme. Technologically this might be exploited for thermoelectrics which rely on a strong electron-hole asymmetry [98–101]. Particularly beneficial are sharp peaks in the spectral function on only one side of the Fermi level [98], as found for the SrO-terminated monolayer, see Fig. 2, within DMFT. There, *local* electronic correlations can enhance thermoelectricity through energy-dependent renormalizations that are different for electrons ( $\omega > 0$ ) and holes ( $\omega < 0$ ) [99,102]. Our finding of a momentum-selectivity in the scattering rate may provide an *additional* route: a particle-hole asymmetry that is driven (or enhanced) by *nonlocal* renormalizations. Indeed,

looking again at the SrO-terminated monolayer, dominant (sub-leading) FM fluctuations at  $n = 1.3$  ( $n = 1.5$ ), drive a dispersive scattering rate [103] that is larger for occupied momenta (“ $k < k_F$ ”) then for empty states (“ $k > k_F$ ”). Specifically, the downward kinks in the  $xz$  component of  $\text{Im}\Sigma$ , see Fig. 6, occur for  $\mathbf{k} = (0, 0)$  and  $\mathbf{k} = (0, \pi)$  which are inside the (DMFT)  $xz$  Fermi surface, see Fig. 2. For  $\mathbf{k} = (\pi, \pi)$  and  $\mathbf{k} = (\pi/2, \pi/2)$ , which are outside the Fermi surface, the  $xz$  scattering rate instead decreases when approaching zero frequency. This electron-hole asymmetry of the scattering time will make the already electronlike DMFT thermopower even more negative, thus increasing its magnitude.

## VII. CONCLUSIONS

Based on simulations of oxide ultrathin films, we demonstrated that, in quasi-two-dimensional systems, strong long-range magnetic (orbital) fluctuations cause a strong (weak to moderate) momentum differentiation in the self-energy. We devised a binaural fluctuation diagnostics tool for analyzing this momentum differentiation, which links the occurrence of strong nonlocal self-energy corrections to an interplay of the size and shape of the Fermi surface and the characteristic momentum transfer of existing fluctuations. Further, we demonstrated that the momentum differentiation from magnetic fluctuations has a much richer structure than the current focus on cuprates and pseudogap physics suggests: Strong variations in renormalizations may not only occur on the Fermi surface but also perpendicular to it. Our results call for a (re)examining—with beyond-DMFT methods—of correlated electron systems that host strong nonlocal fluctuations: layered materials as well as ultrathin oxide films and heterostructures.

## ACKNOWLEDGMENTS

We thank M. Fuchs, A. Galler, J. Kaufmann, G. Sangiovanni, P. Thunström, A. Toschi, and Z. Zhong for fruitful discussions. The authors acknowledge support from the Austrian Science Fund (FWF) through Grants No. P 32044 and No. P 30213. Calculations were performed on the Vienna Scientific Cluster (VSC).

- 
- [1] Y. M. Vilks and A.-M. S. Tremblay, Non-perturbative many-body approach to the Hubbard model and single-particle pseudogap, *J. Phys. I (France)* **7**, 1309 (1997).
  - [2] G. Rohringer, A. Toschi, A. Katanin, and K. Held, Critical Properties of the Half-Filled Hubbard Model in Three Dimensions, *Phys. Rev. Lett.* **107**, 256402 (2011).
  - [3] G. Rohringer and A. Toschi, Impact of non-local correlations over different energy scales: A dynamical vertex approximation study, *Phys. Rev. B* **94**, 125144 (2016).
  - [4] M. R. Norman, H. Ding, M. Randeria, J. C. Campuzano, T. Yokoya, T. Takeuchi, T. Takahashi, T. Mochiku, K. Kadowaki, P. Guptasarma, and D. G. Hinks, Destruction of the Fermi surface in underdoped high-Tc superconductors, *Nature (London)* **392**, 157 (1998).
  - [5] T. Timusk and B. Statt, The pseudogap in high-temperature superconductors: An experimental survey, *Rep. Prog. Phys.* **62**, 61 (1999).
  - [6] M. R. Norman, D. Pines, and C. Kallin, The pseudogap: Friend or foe of high Tc ? *Adv. Phys.* **54**, 715 (2005).
  - [7] B. Keimer, S. A. Kivelson, M. R. Norman, S. Uchida, and J. Zaanen, From quantum matter to high-temperature superconductivity in copper oxides, *Nature (London)* **518**, 179 (2015).
  - [8] A. P. Kampf and J. R. Schrieffer, Spectral function and photoemission spectra in antiferromagnetically correlated metals, *Phys. Rev. B* **42**, 7967 (1990).
  - [9] Y. M. Vilks and A.-M. S. Tremblay, Destruction of Fermi-liquid quasiparticles in two dimensions by critical fluctuations, *Europhys. Lett.* **33**, 159 (1996).

- [10] D. Rost, E. V. Gorelik, F. Assaad, and N. Blümer, Momentum-dependent pseudogaps in the half-filled two-dimensional Hubbard model, *Phys. Rev. B* **86**, 155109 (2012).
- [11] B. Kyung, V. Hankevych, A.-M. Daré, and A.-M. S. Tremblay, Pseudogap and Spin Fluctuations in the Normal State of the Electron-Doped Cuprates, *Phys. Rev. Lett.* **93**, 147004 (2004).
- [12] E. Gull, O. Parcollet, and A. J. Millis, Superconductivity and the Pseudogap in the Two-Dimensional Hubbard Model, *Phys. Rev. Lett.* **110**, 216405 (2013).
- [13] O. Cyr-Choinière, R. Daou, F. Laliberté, C. Collignon, S. Badoux, D. LeBoeuf, J. Chang, B. J. Ramshaw, D. A. Bonn, W. N. Hardy, R. Liang, J.-Q. Yan, J.-G. Cheng, J.-S. Zhou, J. B. Goodenough, S. Pyon, T. Takayama, H. Takagi, N. Doiron-Leyraud, and L. Taillefer, Pseudogap temperature  $T^*$  of cuprate superconductors from the Nernst effect, *Phys. Rev. B* **97**, 064502 (2018).
- [14] A. Kampf and J. R. Schrieffer, Pseudogaps and the spin-bag approach to high- $T_c$  superconductivity, *Phys. Rev. B* **41**, 6399 (1990).
- [15] P. Monthoux and D. Pines,  $\text{YBa}_2\text{Cu}_3\text{O}_7$ : A nearly antiferromagnetic Fermi liquid, *Phys. Rev. B* **47**, 6069 (1993).
- [16] A. Abanov, A. V. Chubukov, and J. Schmalian, Quantum-critical theory of the spin-fermion model and its application to cuprates: Normal state analysis, *Adv. Phys.* **52**, 119 (2003).
- [17] Y. M. Vil'k, Shadow features and shadow bands in the paramagnetic state of cuprate superconductors, *Phys. Rev. B* **55**, 3870 (1997).
- [18] W. Wu, M. S. Scheurer, M. Ferrero, and A. Georges, Effect of van Hove singularities in the onset of pseudogap states in Mott insulators, *Phys. Rev. Res.* **2**, 033067 (2020).
- [19] J. González, F. Guinea, and M. A. H. Vozmediano, Kinematics of Electrons near a Van Hove Singularity, *Phys. Rev. Lett.* **84**, 4930 (2000).
- [20] C. J. Halboth and W. Metzner,  $d$ -Wave Superconductivity and Pomeranchuk Instability in the Two-Dimensional Hubbard Model, *Phys. Rev. Lett.* **85**, 5162 (2000).
- [21] C. Honerkamp and M. Salmhofer, Magnetic and Superconducting Instabilities of the Hubbard Model at the Van Hove Filling, *Phys. Rev. Lett.* **87**, 187004 (2001).
- [22] F. Krien, P. Worm, P. Chalupa, A. Toschi, and K. Held, Spin scattering turns complex at strong coupling: The key to pseudogap and Fermi arcs in the Hubbard model, [arXiv:2107.06529](https://arxiv.org/abs/2107.06529).
- [23] D. Fay, O. Loesener, and J. Appel, Momentum-dependent electron self-energy in nearly ferromagnetic systems: Comparison of spin fluctuations and phonons, *Phys. Rev. B* **37**, 3299 (1988).
- [24] P. Monthoux, Migdal's theorem and the pseudogap, *Phys. Rev. B* **68**, 064408 (2003).
- [25] V. Hankevych, B. Kyung, and A.-M. S. Tremblay, Weak ferromagnetism and other instabilities of the two-dimensional  $t - t'$  Hubbard model at van Hove fillings, *Phys. Rev. B* **68**, 214405 (2003).
- [26] A. A. Katanin, A. P. Kampf, and V. Y. Irkhin, Anomalous self-energy and Fermi surface quasisplitting in the vicinity of a ferromagnetic instability, *Phys. Rev. B* **71**, 085105 (2005).
- [27] A. A. Katanin, Electronic self-energy and triplet pairing fluctuations in the vicinity of a ferromagnetic instability in two-dimensional systems: Quasistatic approach, *Phys. Rev. B* **72**, 035111 (2005).
- [28] M. Pickem, J. Kaufmann, K. Held, and J. M. Tomczak, Zoology of spin and orbital fluctuations in ultrathin oxide films, *Phys. Rev. B* **104**, 024307 (2021).
- [29] B. Klebel-Knobloch, T. Schäfer, A. Toschi, and J. M. Tomczak, Anisotropy of electronic correlations: On the applicability of local theories to layered materials, *Phys. Rev. B* **103**, 045121 (2021).
- [30] Y.-M. Xu, P. Richard, K. Nakayama, T. Kawahara, Y. Sekiba, T. Qian, M. Neupane, S. Souma, T. Sato, T. Takahashi, H.-Q. Luo, H.-H. Wen, G.-F. Chen, N.-L. Wang, Z. Wang, Z. Fang, X. Dai, and H. Ding, Fermi surface dichotomy of the superconducting gap and pseudogap in underdoped pnictides, *Nat. Commun.* **2**, 392 (2011).
- [31] S. J. Moon, A. A. Schafgans, S. Kasahara, T. Shibauchi, T. Terashima, Y. Matsuda, M. A. Tanatar, R. Prozorov, A. Thaler, P. C. Canfield, A. S. Sefat, D. Mandrus, and D. N. Basov, Infrared Measurement of the Pseudogap of P-Doped and Co-Doped High-Temperature  $\text{BaFe}_2\text{As}_2$  Superconductors, *Phys. Rev. Lett.* **109**, 027006 (2012).
- [32] X. Zhou, P. Cai, A. Wang, W. Ruan, C. Ye, X. Chen, Y. You, Z.-Y. Weng, and Y. Wang, Evolution from Unconventional Spin Density Wave to Superconductivity and a Pseudogaplike Phase in  $\text{NaFe}_{1-x}\text{Co}_x\text{As}$ , *Phys. Rev. Lett.* **109**, 037002 (2012).
- [33] T. Shimojima, T. Sonobe, W. Malaeb, K. Shinada, A. Chainani, S. Shin, T. Yoshida, S. Ideta, A. Fujimori, H. Kumigashira, K. Ono, Y. Nakashima, H. Anzai, M. Arita, A. Ino, H. Namatame, M. Taniguchi, M. Nakajima, S. Uchida, Y. Tomioka *et al.*, Pseudogap formation above the superconducting dome in iron pnictides, *Phys. Rev. B* **89**, 045101 (2014).
- [34] P.-H. Lin, Y. Texier, A. Taleb-Ibrahimi, P. Le Fèvre, F. Bertran, E. Giannini, M. Grioni, and V. Brouet, Nature of the Bad Metallic Behavior of  $\text{Fe}_{1.06}\text{Te}$  Inferred from its Evolution in the Magnetic State, *Phys. Rev. Lett.* **111**, 217002 (2013).
- [35] M. Uchida, K. Ishizaka, P. Hansmann, Y. Kaneko, Y. Ishida, X. Yang, R. Kumai, A. Toschi, Y. Onose, R. Arita, K. Held, O. K. Andersen, S. Shin, and Y. Tokura, Pseudogap of Metallic Layered Nickelate  $R_{2-x}\text{Sr}_x\text{NiO}_4$  ( $R = \text{Nd, Eu}$ ) Crystals Measured using Angle-Resolved Photoemission Spectroscopy, *Phys. Rev. Lett.* **106**, 027001 (2011).
- [36] Y. K. Kim, O. Krupin, J. D. Denlinger, A. Bostwick, E. Rotenberg, Q. Zhao, J. F. Mitchell, J. W. Allen, and B. J. Kim, Fermi arcs in a doped pseudospin-1/2 Heisenberg antiferromagnet, *Science* **345**, 187 (2014).
- [37] I. H. Inoue, O. Goto, H. Makino, N. E. Hussey, and M. Ishikawa, Bandwidth control in a perovskite-type  $3d^1$ -correlated metal  $\text{Ca}_{1-x}\text{Sr}_x\text{VO}_3$ . i. evolution of the electronic properties and effective mass, *Phys. Rev. B* **58**, 4372 (1998).
- [38] S.-K. Mo, J. D. Denlinger, H.-D. Kim, J.-H. Park, J. W. Allen, A. Sekiyama, A. Yamasaki, K. Kadono, S. Suga, Y. Saitoh, T. Muro, P. Metcalf, G. Keller, K. Held, V. Eyert, V. I. Anisimov, and D. Vollhardt, Prominent Quasiparticle Peak in the Photoemission Spectrum of the Metallic Phase of  $\text{V}_2\text{O}_3$ , *Phys. Rev. Lett.* **90**, 186403 (2003).
- [39] I. A. Nekrasov, K. Held, G. Keller, D. E. Kondakov, T. Pruschke, M. Kollar, O. K. Andersen, V. I. Anisimov, and D. Vollhardt, Momentum-resolved spectral functions of  $\text{SrVO}_3$  calculated by LDA + DMFT, *Phys. Rev. B* **73**, 155112 (2006).

- [40] K. Byczuk, M. Kollar, K. Held, Y. F. Yang, I. A. Nekrasov, T. Pruschke, and D. Vollhardt, Kinks in the dispersion of strongly correlated electrons, *Nat. Phys.* **3**, 168 (2007).
- [41] K. Held, R. Peters, and A. Toschi, Poor Man's Understanding of Kinks Originating from Strong Electronic Correlations, *Phys. Rev. Lett.* **110**, 246402 (2013).
- [42] K. Yoshimatsu, T. Okabe, H. Kumigashira, S. Okamoto, S. Aizaki, A. Fujimori, and M. Oshima, Dimensional-Crossover-Driven Metal-Insulator Transition in SrVO<sub>3</sub> Ultrathin Films, *Phys. Rev. Lett.* **104**, 147601 (2010).
- [43] M. Kobayashi, K. Yoshimatsu, T. Mitsuhashi, M. Kitamura, E. Sakai, R. Yukawa, M. Minohara, A. Fujimori, K. Horiba, and H. Kumigashira, Emergence of quantum critical behavior in metallic quantum-well states of strongly correlated oxides, *Sci. Rep.* **7**, 16621 (2017).
- [44] Z. Zhong, M. Wallerberger, J. M. Tomczak, C. Taranto, N. Parragh, A. Toschi, G. Sangiovanni, and K. Held, Electronics with Correlated Oxides: SrVO<sub>3</sub>/SrTiO<sub>3</sub> as a Mott Transistor, *Phys. Rev. Lett.* **114**, 246401 (2015).
- [45] M. Gu, S. Wolf, and J. Lu, Two-dimensional Mott insulators in SrVO<sub>3</sub> ultrathin films, *Adv. Mater. Interfaces* **1**, 1300126 (2014).
- [46] Y. Okada, S.-Y. Shiao, T.-R. Chang, G. Chang, M. Kobayashi, R. Shimizu, H.-T. Jeng, S. Shiraki, H. Kumigashira, A. Bansil, H. Lin, and T. Hitosugi, Quasiparticle Interference on Cubic Perovskite Oxide Surfaces, *Phys. Rev. Lett.* **119**, 086801 (2017).
- [47] J. Gabel, M. Pickem, P. Scheiderer, L. Dudy, B. Leikert, M. Fuchs, M. Stübinger, M. Schmitt, J. Küspert, G. Sangiovanni, J. M. Tomczak, K. Held, T.-L. Lee, R. Claessen, and M. Sing, Toward functionalized ultrathin oxide films: The impact of surface apical oxygen, *Adv. Electron. Mater.* **8**, 2101006 (2021).
- [48] W. Metzner and D. Vollhardt, Correlated Lattice Fermions in  $d = \infty$  Dimensions, *Phys. Rev. Lett.* **62**, 324 (1989).
- [49] A. Georges and G. Kotliar, Hubbard model in infinite dimensions, *Phys. Rev. B* **45**, 6479 (1992).
- [50] A. Georges, G. Kotliar, W. Krauth, and M. J. Rozenberg, Dynamical mean-field theory of strongly correlated fermion systems and the limit of infinite dimensions, *Rev. Mod. Phys.* **68**, 13 (1996).
- [51] A. Toschi, A. A. Katanin, and K. Held, Dynamical vertex approximation: A step beyond dynamical mean-field theory, *Phys. Rev. B* **75**, 045118 (2007).
- [52] A. A. Katanin, A. Toschi, and K. Held, Comparing pertinent effects of antiferromagnetic fluctuations in the two- and three-dimensional Hubbard model, *Phys. Rev. B* **80**, 075104 (2009).
- [53] A. Galler, P. Thunström, P. Gunacker, J. M. Tomczak, and K. Held, Ab initio, *Phys. Rev. B* **95**, 115107 (2017).
- [54] G. Rohringer, H. Hafermann, A. Toschi, A. A. Katanin, A. E. Antipov, M. I. Katsnelson, A. I. Lichtenstein, A. N. Rubtsov, and K. Held, Diagrammatic routes to nonlocal correlations beyond dynamical mean field theory, *Rev. Mod. Phys.* **90**, 025003 (2018).
- [55] R. W. Godby, M. Schlüter, and L. J. Sham, Self-energy operators and exchange-correlation potentials in semiconductors, *Phys. Rev. B* **37**, 10159 (1988).
- [56] T. Miyake, C. Martins, R. Sakuma, and F. Aryasetiawan, Effects of momentum-dependent self-energy in the electronic structure of correlated materials, *Phys. Rev. B* **87**, 115110 (2013).
- [57] J. M. Tomczak, M. Casula, T. Miyake, and S. Biermann, Asymmetry in band widening and quasiparticle lifetimes in SrVO<sub>3</sub>: Competition between screened exchange and local correlations from combined GW and dynamical mean-field theory GW + DMFT, *Phys. Rev. B* **90**, 165138 (2014).
- [58] P. Blaha, K. Schwarz, G. K. H. Madsen, D. Kvasnicka, J. Luitz, R. Laskowski, F. Tran, and L. D. Marks, WIEN2k, *An Augmented Plane Wave + Local Orbitals Program for Calculating Crystal Properties* (Karlheinz Schwarz, Techn. Universität Wien, Austria, 2018), [http://www.wien2k.at/reg\\_user/textbooks/usersguide.pdf](http://www.wien2k.at/reg_user/textbooks/usersguide.pdf).
- [59] P. Blaha, K. Schwarz, F. Tran, R. Laskowski, G. K. H. Madsen, and L. D. Marks, WIEN2k: An APW+lo program for calculating the properties of solids, *J. Chem. Phys.* **152**, 074101 (2020).
- [60] J. P. Perdew, K. Burke, and M. Ernzerhof, Generalized Gradient Approximation Made Simple, *Phys. Rev. Lett.* **77**, 3865 (1996).
- [61] C. Wang, H. Zhang, K. Deepak, C. Chen, A. Fouchet, J. Duan, D. Hilliard, U. Kentsch, D. Chen, M. Zeng, X. Gao, Y.-J. Zeng, M. Helm, W. Prellier, and S. Zhou, Tuning the metal-insulator transition in epitaxial SrVO<sub>3</sub> films by uniaxial strain, *Phys. Rev. Mater.* **3**, 115001 (2019).
- [62] J. Kuneš, R. Arita, P. Wissgott, A. Toschi, H. Ikeda, and K. Held, Wien2wannier: From linearized augmented plane waves to maximally localized Wannier functions, *Comput. Phys. Commun.* **181**, 1888 (2010).
- [63] A. A. Mostofi, J. R. Yates, Y.-S. Lee, I. Souza, D. Vanderbilt, and N. Marzari, wannier90: A tool for obtaining maximally-localised Wannier functions, *Comput. Phys. Commun.* **178**, 685 (2008).
- [64] K. Held, Electronic structure calculations using dynamical mean field theory, *Adv. Phys.* **56**, 829 (2007).
- [65] J. Kaufmann and K. Held, ana\_cont: Python package for analytic continuation, *Comp. Phys. Commun.* **282**, 108519 (2022).
- [66] J. M. Tomczak, P. Liu, A. Toschi, G. Kresse, and K. Held, Merging GW with DMFT and non-local correlations beyond, *Eur. Phys. J.: Spec. Top.* **226**, 2565 (2017).
- [67] A. Galler, J. Kaufmann, P. Gunacker, M. Pickem, P. Thunström, J. M. Tomczak, and K. Held, Towards ab initio calculations with the dynamical vertex approximation, *J. Phys. Soc. Jpn.* **87**, 041004 (2018).
- [68] A. Galler, P. Thunström, J. Kaufmann, M. Pickem, J. M. Tomczak, and K. Held, The AbinitioDΓA project v1.0: Non-local correlations beyond and susceptibilities within dynamical mean-field theory, *Comput. Phys. Commun.* **245**, 106847 (2019).
- [69] H. Kusunose, Influence of spatial correlations in strongly correlated electron systems: Extension to dynamical mean field approximation, *J. Phys. Soc. Jpn.* **75**, 054713 (2006).
- [70] A. N. Rubtsov, M. I. Katsnelson, and A. I. Lichtenstein, Dual fermion approach to nonlocal correlations in the Hubbard model, *Phys. Rev. B* **77**, 033101 (2008).
- [71] G. Rohringer, A. Toschi, H. Hafermann, K. Held, V. I. Anisimov, and A. A. Katanin, One-particle irreducible functional approach: A route to diagrammatic extensions of

- the dynamical mean-field theory, *Phys. Rev. B* **88**, 115112 (2013).
- [72] C. Taranto, S. Andergassen, J. Bauer, K. Held, A. Katanin, W. Metzner, G. Rohringer, and A. Toschi, From Infinite to Two Dimensions through the Functional Renormalization Group, *Phys. Rev. Lett.* **112**, 196402 (2014).
- [73] G. Li, Hidden physics in the dual-fermion approach: A special case of a nonlocal expansion scheme, *Phys. Rev. B* **91**, 165134 (2015).
- [74] O. Parcollet, M. Ferrero, T. Ayrál, H. Hafermann, I. Krivenko, L. Messio, and P. Seth, Triqs: A toolbox for research on interacting quantum systems, *Comput. Phys. Commun.* **196**, 398 (2015).
- [75] G. Sordi, K. Haule, and A.-M. S. Tremblay, Mott physics and first-order transition between two metals in the normal-state phase diagram of the two-dimensional Hubbard model, *Phys. Rev. B* **84**, 075161 (2011).
- [76] S. Sakai, G. Sangiovanni, M. Civelli, Y. Motome, K. Held, and M. Imada, Cluster-size dependence in cellular dynamical mean-field theory, *Phys. Rev. B* **85**, 035102 (2012).
- [77] T. Schäfer, A. Toschi, and K. Held, Dynamical vertex approximation for the two-dimensional Hubbard model, *J. Magn. Mater.* **400**, 107 (2016).
- [78] T. Schäfer, F. Geles, D. Rost, G. Rohringer, E. Arrighoni, K. Held, N. Blümer, M. Aichhorn, and A. Toschi, Fate of the false Mott-Hubbard transition in two dimensions, *Phys. Rev. B* **91**, 125109 (2015).
- [79] O. Gunnarsson, T. Schäfer, J. P. F. LeBlanc, E. Gull, J. Merino, G. Sangiovanni, G. Rohringer, and A. Toschi, Fluctuation Diagnostics of the Electron Self-Energy: Origin of the Pseudogap Physics, *Phys. Rev. Lett.* **114**, 236402 (2015).
- [80] J. Gukelberger, E. Kozik, and H. Hafermann, Diagrammatic Monte Carlo approach for diagrammatic extensions of dynamical mean-field theory: Convergence analysis of the dual fermion technique, *Phys. Rev. B* **96**, 035152 (2017).
- [81] T. Schäfer, N. Wentzell, F. Šimković, Y.-Y. He, C. Hille, M. Klett, C. J. Eckhardt, B. Arzhang, V. Harkov, F. M. Le Régent, A. Kirsch, Y. Wang, A. J. Kim, E. Kozik, E. A. Stepanov, A. Kauch, S. Andergassen, P. Hansmann, D. Rohe, Y. M. Vilk *et al.*, Tracking the Footprints of Spin Fluctuations: A MultiMethod, MultiMessenger Study of the Two-Dimensional Hubbard Model, *Phys. Rev. X* **11**, 011058 (2021).
- [82] A. E. Antipov, E. Gull, and S. Kirchner, Critical Exponents of Strongly Correlated Fermion Systems from Diagrammatic Multiscale Methods, *Phys. Rev. Lett.* **112**, 226401 (2014).
- [83] T. Schäfer, A. A. Katanin, K. Held, and A. Toschi, Interplay of Correlations and Kohn Anomalies in Three Dimensions: Quantum Criticality with a Twist, *Phys. Rev. Lett.* **119**, 046402 (2017).
- [84] T. Schäfer, A. A. Katanin, M. Kitatani, A. Toschi, and K. Held, Quantum Criticality in the Two-Dimensional Periodic Anderson Model, *Phys. Rev. Lett.* **122**, 227201 (2019).
- [85] P. Werner, A. Comanac, L. de' Medici, M. Troyer, and A. J. Millis, Continuous-Time Solver for Quantum Impurity Models, *Phys. Rev. Lett.* **97**, 076405 (2006).
- [86] E. Gull, A. J. Millis, A. I. Lichtenstein, A. N. Rubtsov, M. Troyer, and P. Werner, Continuous-time Monte Carlo methods for quantum impurity models, *Rev. Mod. Phys.* **83**, 349 (2011).
- [87] M. Wallerberger, A. Hausoel, P. Gunacker, A. Kowalski, N. Parragh, F. Goth, K. Held, and G. Sangiovanni, w2dynamics: Local one- and two-particle quantities from dynamical mean field theory, *Comput. Phys. Commun.* **235**, 388 (2019).
- [88] P. Gunacker, M. Wallerberger, E. Gull, A. Hausoel, G. Sangiovanni, and K. Held, Continuous-time quantum Monte Carlo using worm sampling, *Phys. Rev. B* **92**, 155102 (2015).
- [89] J. Kaufmann, C. Eckhardt, M. Pickem, M. Kitatani, A. Kauch, and K. Held, Self-consistent ladder dynamical vertex approximation, *Phys. Rev. B* **103**, 035120 (2021).
- [90] O. Gunnarsson, E. Koch, and R. M. Martin, Mott transition in degenerate Hubbard models: Application to doped fullerenes, *Phys. Rev. B* **54**, R11026 (1996).
- [91] E. Pavarini, S. Biermann, A. Poteryaev, A. I. Lichtenstein, A. Georges, and O. K. Andersen, Mott Transition and Suppression of Orbital Fluctuations in Orthorhombic  $3d^1$  Perovskites, *Phys. Rev. Lett.* **92**, 176403 (2004).
- [92] E. Pavarini, I. Dasgupta, T. Saha-Dasgupta, O. Jepsen, and O. K. Andersen, Band-Structure Trend in Hole-Doped Cuprates and Correlation with  $T_{cmax}$ , *Phys. Rev. Lett.* **87**, 047003 (2001).
- [93] K. Held and D. Vollhardt, Microscopic conditions favoring itinerant ferromagnetism: Hund's rule coupling and orbital degeneracy, *Eur. Phys. J. B* **5**, 473 (1998).
- [94] T. Schäfer, A. Toschi, and J. M. Tomczak, Separability of dynamical and nonlocal correlations in three dimensions, *Phys. Rev. B* **91**, 121107(R) (2015).
- [95] T. Schäfer and A. Toschi, How to read between the lines of electronic spectra: The diagnostics of fluctuations in strongly correlated electron systems, *J. Phys.: Condens. Matter* **33**, 214001 (2021).
- [96] L. Del Re and G. Rohringer, Fluctuations analysis of spin susceptibility: Néel ordering revisited in dynamical mean field theory, *Phys. Rev. B* **104**, 235128 (2021).
- [97] See Supplemental Material at <http://link.aps.org/supplemental/10.1103/PhysRevResearch.4.033253> for an animated decomposition of self-energy corrections and their momentum-space contributions along a  $k$  path.
- [98] G. Mahan and J. Sofo, The best thermoelectric, *Proc. Natl. Acad. Sci. U.S.A.* **93**, 7436 (1996).
- [99] K. Held, R. Arita, V. I. Anisimov, and K. Kuroki, The LDA+DMFT route to identify good thermoelectrics, in *Properties and Applications of Thermoelectric Materials*, NATO Science for Peace and Security Series B: Physics and Biophysics, edited by V. Zlatić and A. Hewson (Springer, Netherlands, 2009), pp. 141–157.
- [100] V. Zlatić and R. Monnier, *Modern Theory of Thermoelectricity* (Oxford University Press, Oxford, United Kingdom, 2014).
- [101] J. M. Tomczak, Thermoelectricity in correlated narrow-gap semiconductors, *J. Phys.: Condens. Matter* **30**, 183001 (2018).
- [102] K. Haule and G. Kotliar, Thermoelectrics near the Mott localization—delocalization transition, in *Properties and Applications of Thermoelectric Materials*, edited by V. Zlatić and A. C. Hewson (Springer Netherlands, Dordrecht, 2009), pp. 119–131.
- [103] P. Sun, W. Xu, J. M. Tomczak, G. Kotliar, M. Søndergaard, B. B. Iversen, and F. Steglich, Highly dispersive electron relaxation and colossal thermoelectricity in the correlated semiconductor  $\text{FeSb}_2$ , *Phys. Rev. B* **88**, 245203 (2013).